J. Fluid Mech. (2001), *vol.* 448, *pp.* 23–51.
DOI: 10.1017/S0022112001005729 Printed in the United Kingdom

Linear stability of co-flowing liquid–gas jets

By J. M. GORDILLO, M. PÉREZ-SABORID AND A. M. GAÑÁN-CALVO

Grupo de Mecánica de Fluidos, Escuela Superior de Ingenieros, Universidad de Sevilla Camino de los Descubrimientos s/n. 41092 Sevilla, Spain

(Received 5 April 2000 and in revised form 14 May 2001)

A temporal, inviscid, linear stability analysis of a liquid jet and the co-flowing gas stream surrounding the jet has been performed. The basic liquid and gas velocity profiles have been computed self-consistently by solving numerically the appropriate set of coupled Navier–Stokes equations reduced using the slenderness approximation. The analysis in the case of a uniform liquid velocity profile recovers the classical Rayleigh and Weber non-viscous results as limiting cases for well-developed and very thin gas boundary layers respectively, but the consideration of realistic liquid velocity profiles brings to light new families of modes which are essential to explain atomization experiments at large enough Weber numbers, and which do not appear in the classical stability analyses of non-viscous parallel streams. In fact, in atomization experiments with Weber numbers around 20, we observe a change in the breakup pattern from axisymmetric to helicoidal modes which are predicted and explained by our theory as having an hydrodynamic origin related to the structure of the liquid-jet basic velocity profile. This work has been motivated by the recent discovery by Gañán-Calvo (1998) of a new atomization technique based on the acceleration to large velocities of coaxial liquid and gas jets by means of a favourable pressure gradient and which are of emerging interest in microfluidic applications (high-quality atomization, micro-fibre production, biomedical applications, etc.).

1. Introduction

The phenomenon of the breaking up of a liquid jet into drops has been investigated both theoretically and experimentally since Rayleigh (1878). In Rayleigh's pioneering theoretical investigation of the phenomenon, a temporal inviscid stability analysis of a liquid cylinder flowing with a uniform velocity was carried out, and the growth rates as function of the wavelength of the perturbation were found. The results deduced from this simple model are found to agree very well with experiments if the velocity of the liquid jet is sufficiently low, because then the breakup process is dominated by capillary effects and the influence of the external air stream can be neglected. At higher relative liquid–gas velocities, such as those common in many atomization processes of technological interest (sprays, fuel injectors, etc.), Rayleigh's results cease to be valid, and the coupling of the liquid jet to the surrounding air must be considered in the stability analysis. The first step in this direction was taken by Weber (1931), who considered the stability of a liquid jet with a coaxial gas stream both flowing with uniform, but different, velocities. His results predicted higher growth rates and shorter breakup wavelengths than those observed in experiments, which led Sterling & Sleicher (1975) to modify Weber's analysis by including viscosity effects through an

ad hoc empirical coefficient in the equations for the perturbations of the gas stream, which was adjusted to fit the experimentally determined curve of the jet breakup length versus jet velocity. A weak point in both Weber's and Sterling & Sleicher's analyses was that of considering highly simplified (uniform) liquid and gas basic flows. In this work we aim to show by a three-step process what the importance is of either the basic liquid or the gas velocity profiles (or both) in the breakup dynamics of co-flowing liquid–gas jets: (i) first we consider the basic velocity profile of the gas only, with a uniform liquid velocity – model A, (ii) then we consider the liquid velocity profile only, with an unperturbed coaxial gas stream – model B, and finally (iii) we consider the velocity profiles of both the liquid and the gas – model C. In this way, our results will show that if basic velocity profiles are computed in a self-consistent manner, it is not necessary to appeal to viscosity effects in the perturbations to explain the observed increase in the breakup lengths (or equivalently, lower growth rates) over those predicted by Weber's theory at high liquid jet velocities.

The stability of liquid jets has also been considered from the point of view of spatial stability theory for both the Rayleigh and Weber problems. Although for the case of open flows, such as mixing and boundary layers over rigid walls, spatial stability results seem to be in better agreement with experiments than those obtained from temporal analyses, for the case of liquid jets at sufficiently high Weber numbers (based on the jet velocity) Keller, Rubinow & Tu (1973) found that for Rayleigh's case both types of analyses lead to essentially the same results; thereafter Lin & Kang (1987) considered the influence of the external gas stream and came to the same conclusion if the Weber number is based on the relative liquid–gas velocity. All the previous models considered uniform liquid and gas velocity profiles, in spite of the analyses performed by Rayleigh (1880) and Miles (1957, 1959*a*, *b*), which pointed out the importance of the role played by the shear layer velocity profile in the development of the instability in an homogeneous medium (Rayleigh) and for the wind generation of waves (Miles). The importance of stability models that account for both liquid and gas basic velocity profiles has been further stressed by Lin & Reitz (1998) and taken into account systematically only in recent works. Thus, Villermaux (1998) has extended the analysis of the stability of a piecewise linear velocity profile performed by Rayleigh to the case in which there exists a density jump across the interface. Due to the much larger momentum of the lighter phase considered in this work, only the velocity profile of the gas shear layer, characterized by its thickness, is considered and a remarkable agreement is found with experimental results. Similarly, Lasheras, Villermaux & Hopfinger (1998) and Lasheras & Hopfinger (2000) have been able to give the scaling of the shedding frequencies observed in their co-flowing liquid–gas experiments through knowledge of the gas shear layer thickness. Another relevant work, more theoretically oriented, is that of Lin & Chen (1998) who performed a spatial stability analysis of an exact solution of the Navier–Stokes equations. In their analysis they took into account both liquid and gas velocity profiles without neglecting viscosity and were able to identify the Rayleigh and Taylor modes of instability for different basic flow regimes and explained, using an energy balance, the sources of energy for the development of each type of instability.

Our work is motivated by the recent discovery by Gañán-Calvo (1998) of a new atomization technique based on the acceleration to large velocities of coaxial liquid and gas jets by means of a favourable pressure gradient. The development of this technique demands an accurate prediction of the droplet-to-jet diameter ratio from the breakup of the laminar capillary microjets produced by that process which have a gas-to-liquid momentum ratio very close to unity. Using a high-speed video camera,

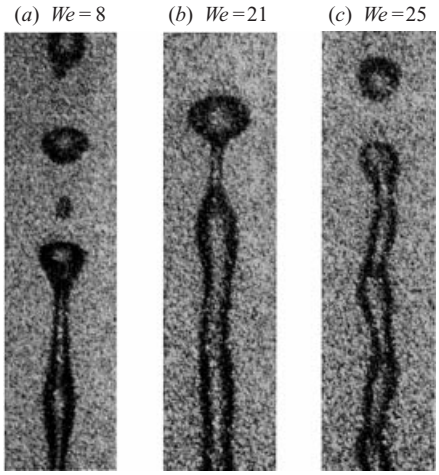

FIGURE 1. Different atomization regimes depending on the value of the Weber number.

we observe that for low Weber numbers, Rayleigh predictions agree with experiments (see figure 1*a*). However, for increasing Weber numbers, our observations (breakup modes) do not agree with any of the existing models assuming uniform gas and liquid velocity profiles. More complete models of liquid jets considering only the actual gas velocity profile (Villermaux 1998), which succeed in predicting frequency breakup of large gas-to-liquid momentum ratio coaxial jets, or models that consider both liquid and gas velocity profiles in a very specific situation (Lin & Chen 1998), are unable to describe satisfactorily the modes observed in our experiments (see figures 1*b* and 1*c*).

These considerations suggest that the observed modes can only be explained by a model of the gas-liquid jet which corresponds more closely to the conditions of our experiments. For that purpose the basic velocity profiles needed for the analysis will be computed self-consistently by solving numerically the parabolized (or, equivalently, the boundary layer type) Navier–Stokes equations. We will then perform a temporal stability analysis since, as pointed out above, it seems justified given the high velocities (high Weber numbers) involved in our problem. According to classical treatments of the stability of parallel flows in the cases in which the instability mechanism is non-viscous, we will neglect the influence of both liquid and gas viscosities in the perturbations by restricting ourselves to large values of the parameter $\omega\lambda^2/\nu_g$ where ω is the frequency of the perturbation, λ its wavelength and ν_g the kinematic viscosity of the gas; neither have we considered the effects of compressibility in both the basic and perturbed flows. These assumptions must be either validated or refuted *a posteriori* after comparison of the theoretical results with experiments. It will be shown that, in spite of the simplifications made, our model is able to explain the different atomization regimes observed in experiments and a rich variety of modes, apparently unexplored in the literature, appear due to the consideration of the structure of basic flow in both the liquid and gas streams; the well-known results for the case of uniform streams are recovered as a limiting case when the thicknesses of the boundary layers which develop in the liquid and the surrounding gas tend to zero.

The structure of the paper is as follows. In § 2 we formulate the equations and boundary conditions governing the basic flow of the liquid and gas stream, and explain the numerical procedure used to solve the problem. In § 3 we analyse the influence of the parameters of the problem and conditions at the initial station (exit of the

pressurized chamber) on the basic solution and make comparisons with experimental results. The stability analysis is formulated in § 4, where the equations governing the perturbations are found and the numerical method to solve for the eigenvalues of the problem is described. As was pointed out above, in order to get better insight into the nature of the different kinds of modes found when the stability equations are applied to the basic liquid and gas flows computed in § 3, we have first solved the stability equations for two simplified models in § 5.1 and § 5.2. The first model considers the stability of a liquid jet with uniform velocity surrounded by a gas stream whose basic structure we compute numerically using the method of § 3. For this model we find three different families of modes: a capillary axisymmetric one, a helicoidal one with excitation frequencies of the order of those of the capillary family, and a third group of modes, which will be called *wake modes*, also of helicoidal nature and whose excitation frequencies are of the order of U_∞/R, where U_∞ is the free-stream gas velocity and R the liquid jet radius. With this simplified model the classical Rayleigh and Kelvin–Helmholtz results are recovered in appropriate limits. In § 5.2 we consider a second model for which the basic velocity profiles are more realistic than those of the previous model in the sense that they already take into account the coupling between the liquid and gas basic flows. The simplification in this model, which considers realistic basic velocity profiles, consists in introducing perturbations in the liquid jet while holding the gas stream unperturbed. We then find, besides the capillary family found in § 5.1, two different families of modes, one axisymmetric and the second one helicoidal, both associated with the velocity gradients in the liquid. The five different families found previously in the simplified models of § 5.1 and § 5.2 are the ones present in the complete model considered in § 5.3, where the more realistic basic velocity profiles computed in § 3 are used. In § 6 we compare the numerical results obtained in § 5.3 with atomization experiments, and it will be shown that our theory explains the general features observed in the jet breakup of our atomization experiments. Finally, conclusions are presented in § 7.

2. Basic solution

The first step in performing the stability analysis is to find the basic velocity profiles for the liquid and gas streams. Figure 2(*a*) is a sketch of the experimental atomization device (Gañán-Calvo 1998) where it can be seen that the diameter of the orifice of the pressurized chamber (of the order of 200 μm) is much larger than that of the liquid jet (of the order of 10 μm). Thus, as a first approach to the problem, it seems reasonable to neglect the effect over the liquid jet of the mixing layer (see figure 2*b*) that develops in the region where gas velocities drop to zero. Therefore, from now on we will focus on the simplified model of figure 2(*c*), where gas velocities at infinity tend to a non-zero constant value. To write the equations which govern the downstream evolution of both the liquid and gas flows we will find it convenient to use the following set of dimensionless parameters and variables:

$$r = \frac{\hat{r}}{R_0}, \quad z = {Re_g}^{-1}\frac{\hat{z}}{R_0}, \quad u = \frac{\hat{u}}{U_\infty}, \quad v = Re_g\frac{\hat{v}}{U_\infty}, \quad f = \frac{\hat{f}}{R_0}, \quad p_l = \frac{\hat{p}_l}{\rho_l {U^2}_\infty}, \tag{2.1}$$

$$We_0 = \frac{\rho_g {U^2}_\infty R_0}{\sigma}, \quad M = \frac{\rho_l}{\rho_g}, \quad \nu = \frac{\nu_l}{\nu_g}, \quad \mu = \frac{\mu_l}{\mu_g}, \tag{2.2}$$

where R_0 is the radius of the jet at the initial station $z = 0$, U_∞ is the velocity of the gas at $r \to \infty$, σ is the liquid–air surface tension, $Re_g = U_\infty R_0/\nu_g$ and We are

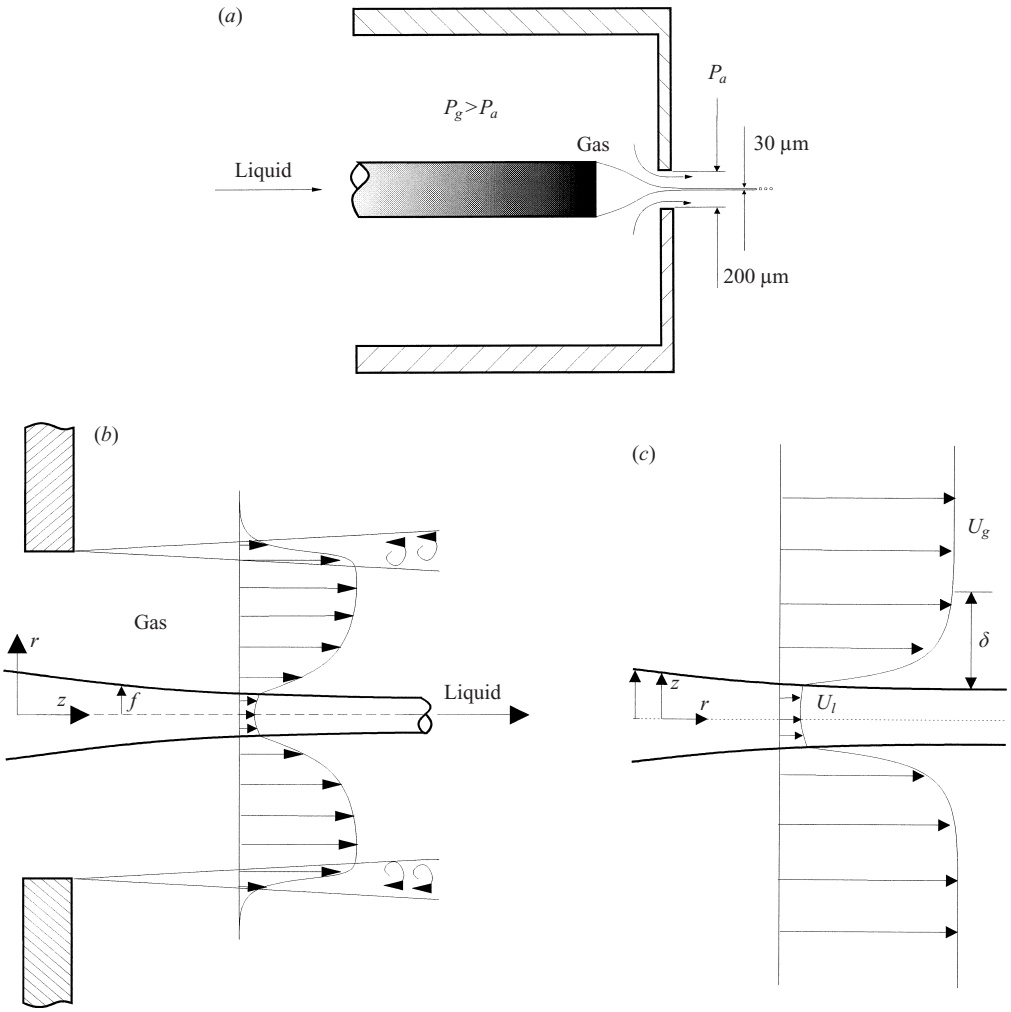

FIGURE 2. Sketch of (*a*) the atomizer; (*b*) the liquid and gas velocity profiles at the exit of the pressurized chamber; (*c*) the velocity profiles considered in this work.

respectively the Reynolds and Weber numbers for the gas flow and $\hat{f}(z)$ is the radius of the liquid jet. Since the geometry is slender, that is $\delta/L \ll 1$ where δ and L are characteristic lengths in the radial and axial directions respectively, the steady Navier–Stokes equations governing the downstream evolution of the gas and liquid streams can be written in the well-known slender (parabolized or boundary-layer) approximation:

$$r\frac{\partial u_g}{\partial z} + \frac{\partial (r v_g)}{\partial r} = 0, \tag{2.3}$$

$$r u_g \frac{\partial u_g}{\partial z} + r v_g \frac{\partial u_g}{\partial r} = \frac{\partial}{\partial r}\left(r\frac{\partial u_g}{\partial r}\right), \tag{2.4}$$

$$\frac{\partial u_l}{\partial z} + \frac{1}{r}\frac{\partial (r v_l)}{\partial r} = 0, \tag{2.5}$$

$$u_l \frac{\partial u_l}{\partial z} + v_l \frac{\partial u_l}{\partial r} = -\frac{\partial p_l}{\partial z} + \nu \frac{1}{r} \frac{\partial}{\partial r} \left(r \frac{\partial u_l}{\partial r} \right), \tag{2.6}$$

$$p_l - p_g = (MWe_0)^{-1} \frac{1}{f}, \tag{2.7}$$

where we have used the variables and parameters defined in (2.1)–(2.2). System (2.3)–(2.7) must be solved subject to the following boundary conditions:

$$z = 0: \quad u_l = u_l(r), \quad u_g = u_g(r), \tag{2.8}$$

$$r = 0: \quad v_l = 0, \quad \frac{\partial u_l}{\partial r} = 0, \tag{2.9}$$

$$v_l = \frac{\partial f}{\partial z} u_l, \tag{2.10}$$

$$r = f: \quad u_g = u_l, \quad v_g = v_l, \quad \frac{\partial u_g}{\partial r} = \mu \frac{\partial u_l}{\partial r}, \tag{2.11}$$

$$r \to \infty: \quad u_g \to 1, \tag{2.12}$$

where condition (2.8) specifies the liquid and gas velocity profiles at the initial station $z = 0$, (2.9) expresses the regularity conditions at the jet axis due to the axial symmetry of the problem, (2.10) and (2.11) express respectively the free surface condition and the continuity of the velocities and shear stress at the jet surface, and (2.12) represents the matching at $r \to \infty$ of the axial gas velocities to that of the external stream. For computational purposes it proves convenient to eliminate the radial velocities v_l and v_g from the momentum equations (2.4) and (2.6) using the continuity equations (2.3) and (2.5) respectively; equations (2.4) and (2.6) then read

$$r u_g \frac{\partial u_g}{\partial z} + \left(r v_g|_{r=f} - \int_f^r r \frac{\partial u_g}{\partial z} \, \mathrm{d}r \right) \frac{\partial u_g}{\partial r} = \frac{\partial}{\partial r} \left(r \frac{\partial u_g}{\partial r} \right), \tag{2.13}$$

$$u_l \frac{\partial u_l}{\partial z} - \frac{1}{r} \left(\int_0^r r \frac{\partial u_l}{\partial z} \, \mathrm{d}r \right) \frac{\partial u_l}{\partial r} = -\frac{\partial p_l}{\partial z} + \nu \frac{1}{r} \frac{\partial}{\partial r} \left(r \frac{\partial u_l}{\partial r} \right). \tag{2.14}$$

Also, it is numerically advantageous to rewrite equation (2.13) in terms of the new independent variables

$$\zeta = \ln(z + z_0), \quad \eta = \frac{r - f}{(z + z_0)^{1/2}}, \tag{2.15}$$

and equation (2.14) in terms of the independent variables

$$\zeta = \ln(z + z_0), \quad \xi = \frac{1}{2} \frac{r^2}{f^2}, \tag{2.16}$$

where z_0 is a constant which will be determined in § 3 from consideration of the appropriate velocity profiles u_l and u_g at the initial station $z = 0$. In terms of the new variables (2.15)–(2.16) equations (2.13) and (2.14) read

$$\begin{aligned} (f + \exp(0.5\zeta)\eta) u_g \frac{\partial u_g}{\partial \zeta} - \left[\int_0^\eta (f + \exp(0.5\zeta)\eta) \frac{\partial u_g}{\partial \zeta} \, \mathrm{d}\eta \right] \frac{\partial u_g}{\partial \eta} \\ = \left[\exp(0.5\zeta) + \frac{1}{2} \int_0^\eta (f + 2\exp(0.5\zeta)\eta) u_g \, \mathrm{d}\eta \right] \frac{\partial u_g}{\partial \eta} \\ + (f + \exp(0.5\zeta)\eta) \frac{\partial^2 u_g}{\partial \eta^2} + \frac{\partial f}{\partial \zeta} \left(\int_0^\eta u_g \, \mathrm{d}\eta \right) \frac{\partial u_g}{\partial \eta}, \end{aligned} \tag{2.17}$$

$$u_l\frac{\partial u_l}{\partial \zeta}-\left(\int_0^{\xi}\frac{\partial u_l}{\partial \zeta}\,\mathrm{d}\xi\right)\frac{\partial u_l}{\partial \xi}=\frac{2\exp(\zeta)}{f^2}v\left(\frac{\partial u_l}{\partial \xi}+\xi\frac{\partial^2 u_l}{\partial \xi^2}\right)$$
$$+\frac{\partial f}{\partial \zeta}\left[\frac{1}{MWe_0 f^2}+\frac{2}{f}\left(\int_0^{\xi}u_l\,\mathrm{d}\xi\right)\frac{\partial u_l}{\partial \xi}\right], \quad (2.18)$$

and the boundary conditions (2.8) and (2.10)–(2.12) become

$$\zeta=\zeta_0=\ln(z_0): \quad u_g=u_g(\eta), \quad u_l=u_l(\xi), \quad (2.19)$$

$$\eta=0, \xi=1/2: \quad u_l=u_g, \quad \frac{\partial u_g}{\partial \eta}=\mu\frac{\exp(0.5\zeta)}{f}\frac{\partial u_l}{\partial \xi}, \quad (2.20)$$

$$2f\frac{\partial f}{\partial \zeta}\int_0^{1/2}u_l\,\mathrm{d}\xi+f^2\int_0^{1/2}\frac{\partial u_l}{\partial \zeta}\,\mathrm{d}\xi=0, \quad (2.21)$$

$$r\to\infty: \quad u_g\to 1. \quad (2.22)$$

Observe that the free surface condition (2.21) can be written as

$$2\frac{\partial f}{\partial \zeta}q+f^3\int_0^{1/2}\frac{\partial u_l}{\partial \zeta}\,\mathrm{d}\xi=0, \quad (2.23)$$

where $q=\int_0^f ru_l\,\mathrm{d}r=f^2\int_0^{1/2}u_l\,\mathrm{d}\xi$ is the dimensionless liquid flow rate. To solve system (2.17)–(2.18) we have employed a method of lines suggested by the parabolic nature of the equations. According to this method a system of ordinary differential equations with ζ as independent variable is obtained by discretizing in (2.17)–(2.18) the radial derivatives and integrals; the resulting system is then integrated with a marching scheme in the axial direction (we have used a variable-step-size Runge–Kutta method). Using centred finite differences for the radial derivatives and discretizing the integrals in (2.17)–(2.18) by the trapezoidal rule we obtain for the gas domain

$$(f+\exp(0.5\zeta)\eta_i)u_{gi}\frac{\partial u_{gi}}{\partial \zeta}$$
$$-\left[\sum_{k=0}^{k=i}(1-0.5\delta_{k0}-0.5\delta_{ki})h_g(f+\exp(0.5\zeta)\eta_k)\frac{\partial u_{gk}}{\partial \zeta}\right]\frac{u_{g(i+1)}-u_{g(i-1)}}{2h_g}$$
$$=\left[\exp(0.5\zeta)+1/2\sum_{k=0}^{k=i}(1-0.5\delta_{k0}-0.5\delta_{ki})h_g(f+2\exp(0.5\zeta)\eta_k)u_{gk}\right]$$
$$\times\frac{u_{g(i+1)}-u_{g(i-1)}}{2h_g}+(f+\exp(0.5\zeta)\eta_i)\frac{u_{g(i+1)}-2u_{gi}+u_{g(i-1)}}{h_g^2}$$
$$+\left[\sum_{k=0}^{k=i}(1-0.5\delta_{k0}-0.5\delta_{ki})h_g u_{gk}\right]\frac{u_{g(i+1)}-u_{g(i-1)}}{2h_g}\frac{\partial f}{\partial \zeta},$$
$$i=1,\ldots G-1, \quad (2.24)$$

where δ_{ij} is the usual δ of Kroenecker, h_g is the discretization step in the gas region and $u_{gG}=1$, and for the liquid domain

$$u_{lj}\frac{\partial u_{lj}}{\partial \zeta}-\left[\sum_{k=0}^{k=j}(1-0.5\delta_{k0}-0.5\delta_{kj})h_l\frac{\partial u_{lk}}{\partial \zeta}\right]\frac{u_{l(j+1)}-u_{l(j-1)}}{2h_l}$$

$$= \frac{2v\exp(\zeta)}{f^2}\left(\frac{u_{l(j+1)}-u_{l(j-1)}}{2h_l}\right)+\frac{2v\exp(\zeta)}{f^2}\left(\xi_j\frac{u_{l(j+1)}-2u_{lj}+u_{l(j-1)}}{h_l^2}\right)$$
$$+\frac{\partial f}{\partial\zeta}\left[\frac{1}{MWe_0f^2}+\frac{2}{f}\left[\sum_{k=0}^{k=j}(1-0.5\delta_{k0}-0.5\delta_{kj})h_lu_{lk}\right]\frac{u_{l(j+1)}-u_{l(j-1)}}{2h_l}\right],$$
$$j=1,\ldots L-1, \tag{2.25}$$

where h_l is the discretization step and G and L are the number of discretization points in the radial direction (lines) for the gas (labelled by the index i) and for the liquid (labelled by the index j) respectively. The equation for the evolution of the velocity at the axis u_{l0}, corresponding to the node $j=0$, can be obtained from (2.18) by making $\xi=0$ and discretizing $\partial u_l/\partial\xi$ using forward second-order differences:

$$u_{l0}\frac{\partial u_{l0}}{\partial\zeta}=\left(\frac{2v\exp(\zeta)}{f^2}\right)\frac{4u_{l1}-3u_{l0}-u_{l2}}{2h_l}+\frac{1}{MWe_0f^2}\frac{\partial f}{\partial\zeta}. \tag{2.26}$$

Also, the equation for the evolution of the velocity at the jet surface ($j=L, i=0$)$u_{g0}=u_{lL}$ can be obtained by taking the ζ-derivative of the second equation in (2.20), that expresses the continuity of the shear stress at the surface,

$$\eta=0,\xi=1/2:\quad 4\frac{\partial u_{1g}}{\partial\zeta}-\frac{\partial u_{2g}}{\partial\zeta}-3\frac{\partial u_{0g}}{\partial\zeta}+F\left(4\frac{\partial u_{l(L-1)}}{\partial\zeta}-\frac{\partial u_{l(L-2)}}{\partial\zeta}-3\frac{\partial u_{lL}}{\partial\zeta}\right)$$
$$-F(4u_{l(L-1)}-u_{l(L-2)}-3u_{lL})\frac{1}{f}\frac{\partial f}{\partial\zeta}$$
$$=-\frac{F}{2}(4u_{l(L-1)}-u_{l(L-2)}-3u_{lL}), \tag{2.27}$$

where $F=\mu h_g\exp(0.5\zeta)/(h_lf)$ and the η-derivatives at the surface have been discretized forward (gas domain) while the ξ-derivatives have been discretized backwards (liquid domain). Finally, the differential equation for $f(\zeta)$ is obtained from (2.23) as

$$f^3\left[\sum_{j=0}^{j=L}(1-0.5\delta_{j0}-0.5\delta_{jL})h_l\frac{\partial u_{lj}}{\partial\zeta}\right]+2\frac{\partial f}{\partial\zeta}q=0. \tag{2.28}$$

System (2.24)–(2.28) must be integrated subjected to the initial condition

$$\zeta=\zeta_0:\quad u_{gi}=u_g(\eta_i),\quad u_{lj}=u_l(\xi_j),\quad i=0...G,\quad j=0\ldots L. \tag{2.29}$$

In order to obtain efficiently the derivatives $\partial u_{gi}/\partial\zeta$ and $\partial u_{lj}/\partial\zeta$ in (2.24)–(2.28), observe that these equations can be expressed in matrix form as

$$\boldsymbol{A}\cdot\frac{\partial\boldsymbol{u}_g}{\partial\zeta}=\boldsymbol{b}_0+\boldsymbol{b}_1\frac{\partial u_{g0}}{\partial\zeta}+\boldsymbol{b}_2\frac{\partial f}{\partial\zeta}, \tag{2.30}$$

$$\boldsymbol{B}\cdot\frac{\partial\boldsymbol{u}_l}{\partial\zeta}=\boldsymbol{c}_0+\boldsymbol{c}_1\frac{\partial f}{\partial\zeta}, \tag{2.31}$$

where $\boldsymbol{A},\boldsymbol{B}$ are lower triangular matrices and $\boldsymbol{b}_0,\boldsymbol{b}_1,\boldsymbol{b}_2,\boldsymbol{c}_0$ and $\boldsymbol{c}_1$ are vectors whose elements depend on the values of $\boldsymbol{u}_g$ and $\boldsymbol{u}_l$ at the given station. Thus, the solution of (2.30) can be obtained as functions of $\partial u_{g0}/\partial\zeta$ and $\partial f/\partial\zeta$ as

$$\frac{\partial\boldsymbol{u}_g}{\partial\zeta}=\frac{\partial\boldsymbol{u}_g^0}{\partial\zeta}+\frac{\partial\boldsymbol{u}_g^1}{\partial\zeta}\frac{\partial u_{g0}}{\partial\zeta}+\frac{\partial\boldsymbol{u}_g^2}{\partial\zeta}\frac{\partial f}{\partial\zeta}, \tag{2.32}$$

where $\partial \boldsymbol{u}_g^0/\partial\zeta, \partial \boldsymbol{u}_g^1/\partial\zeta$ and $\partial \boldsymbol{u}_g^2/\partial\zeta$ are the solutions of $\boldsymbol{A}\cdot\partial \boldsymbol{u}_g^0/\partial\zeta = \boldsymbol{b}_0, \boldsymbol{A}\cdot\partial \boldsymbol{u}_g^1/\partial\zeta = \boldsymbol{b}_1$ and $\boldsymbol{A}\cdot\partial \boldsymbol{u}_g^2/\partial\zeta = \boldsymbol{b}_2$ respectively. Similarly the solutions of (2.31) can be obtained as a function of $\partial f/\partial\zeta$ as

$$\frac{\partial \boldsymbol{u}_l}{\partial\zeta} = \frac{\partial \boldsymbol{u}_l^0}{\partial\zeta} + \frac{\partial \boldsymbol{u}_l^1}{\partial\zeta}\frac{\partial f}{\partial\zeta}, \tag{2.33}$$

where $\partial \boldsymbol{u}_l^0/\partial\zeta$ and $\partial \boldsymbol{u}_l^1/\partial\zeta$ are the solutions of $\boldsymbol{B}\cdot\partial \boldsymbol{u}_l^0/\partial\zeta = \boldsymbol{c}_0$ and $\boldsymbol{B}\cdot\partial \boldsymbol{u}_l^1/\partial\zeta = \boldsymbol{c}_1$ respectively. Finally, the values of $\partial u_{g0}/\partial\zeta$ and $\partial f/\partial\zeta$ are obtained by substituting the results of (2.32) and (2.33) into equations (2.27) and (2.28). Observe that $\partial \boldsymbol{u}_g^0/\partial\zeta, \partial \boldsymbol{u}_g^1/\partial\zeta$, $\partial \boldsymbol{u}_g^2/\partial\zeta$ and $\partial \boldsymbol{u}_l^0/\partial\zeta, \partial \boldsymbol{u}_l^1/\partial\zeta$ can be obtained very efficiently since $\boldsymbol{A}$ and $\boldsymbol{B}$ are lower triangular. In order to start up the numerical integration it is, of course, necessary to specify velocity profiles for both the liquid and the gas at the initial station $z = 0$. The problem of the initial conditions will be discussed at length in the next section.

3. Numerical and experimental results for the basic flow

Equations (2.24)–(2.28) show that the downstream evolution of the liquid–gas flow depends on the parameters MWe_0, the ratios of the kinematic and dynamic viscosities, ν and μ respectively, as well as on the initial conditions at the initial station $z = 0$. In order to reduce the dimension of the parametric space, we will restrict ourselves, without loss of generality, to the representative case of atomization of water into air. Therefore, the parameter μ will be fixed and, to simplify further the model, ν will also be considered as constant, which means that the modification of this parameter due to variations in the density of the gas at the exit of the atomizer, which are produced by the different pressures used in experiments, will be neglected. Thus, we will consider only the influence on the basic flow of the parameter MWe_0 and of the initial conditions, which will be discussed next.

To obtain the exact boundary conditions at the initial station one should solve the complicated problem of the evolution of the gas–liquid flow from the pressurized chamber up to the exit orifice (initial station $z = 0$ for our problem), a task which is obviously outside the scope of this work. Instead, we have considered physically plausible initial conditions for the velocity profiles of both the gas and the liquid each containing a free parameter, related to the respective thicknesses of the boundary layers which have been adjusted by comparing the computed profiles with the ones observed experimentally. In effect, the acceleration of the flow from the pressurized chamber up to the exit orifice (see figure 2*a*) can be considered nearly isentropic, since the residence time of the fluid particles in the entrance region is so short that viscosity effects remain confined to a narrow region near to the gas–liquid boundary. Therefore we will assume that the initial liquid velocity profile is flat except in an annular region next to the surface where it is assumed to be parabolic, namely

$$u_l = u_c, \quad 0 \leqslant \xi \leqslant \tfrac{1}{2}(1-\Delta)^2, \tag{3.1}$$

$$u_l = u_c + A[\xi - \tfrac{1}{2}(1-\Delta)^2], \quad \tfrac{1}{2}(1-\Delta)^2 \leqslant \xi \leqslant \tfrac{1}{2}, \tag{3.2}$$

where u_c, which is not a free parameter, can be computed in terms of the pressure difference between the pressurized chamber and the atmosphere by simply using Bernouilli's equation (isentropic acceleration of the jet centreline), Δ is a free parameter which determines the thickness of the region where the profile is not constant, and A will be determined from the boundary conditions at the jet surface. In the same vein,

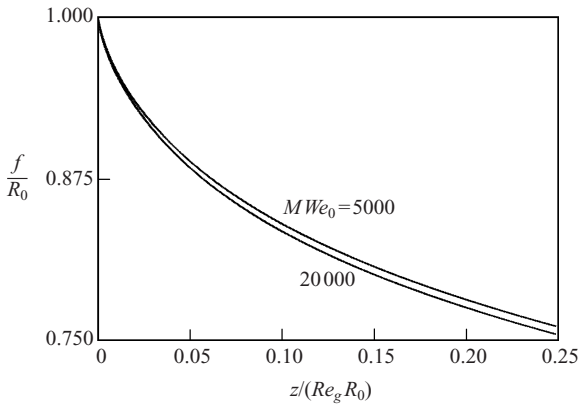

FIGURE 3. Downstream evolution of the liquid jet radius at $MWe_0 = 5000$ and 20 000.

we will assume a Blasius-type profile for the gas boundary condition at $z = 0$, which is obtained from (2.17) in the limit of $\zeta \to -\infty$ and $\partial f/\partial\zeta = 0$, namely

$$\frac{\partial^2 u_g}{\partial \eta^2} + \frac{1}{2}\left(\int_0^\eta u_g \, \mathrm{d}\eta\right)\frac{\partial u_g}{\partial \eta} = 0, \quad \eta > 0, \tag{3.3}$$

which must be integrated in η subject to the boundary conditions (2.20)

$$\eta = 0: \quad u_g = u_l = u_c + A[\tfrac{1}{2} - \tfrac{1}{2}(1-\Delta)^2], \quad \frac{\partial u_g}{\partial \eta} = \frac{\exp(0.5\zeta_0)}{f}\mu\frac{\partial u_l}{\partial \xi} = \frac{A}{f}\exp(0.5\zeta_0)\mu \tag{3.4}$$

where $f = 1$ in the above formulas. Condition $u_g(\eta \to \infty) \to 1$ determines A in (3.4) for fixed values of the free parameters Δ and ζ_0 ($z_0 = \exp(\zeta_0)$). Notice that the gas velocity at infinity is known from the compressible isentropic expansion from the stagnant pressure in the chamber up to the atmospheric pressure at the nozzle exit.

To analyse the influence of the Weber number on the basic flow, we have integrated (2.24)–(2.28) for a given initial condition of the form (3.1)–(3.4) for several values of MWe_0 lying in the range $5000 < MWe_0 < 20\,000$. Figure 3 shows how weakly the basic flows depend on this parameter; therefore we will fix $MWe_0 = 10\,000$, and focus in the following on the assumed initial conditions (3.1)–(3.4) by performing a sensitivity analysis with respect to the parameters Δ and ζ_0.

Figure 4(*b*) shows the influence on the development of the flow of the initial liquid velocity profiles shown in figure 4(*a*) for a fixed value of ζ_0. It can be observed that the liquid jet radius decreases slower for larger Δ (thickness of the liquid boundary layer) since the initial liquid velocities are higher (and consequently also the jet axial momentum) at the jet surface. The evolution of the jet is represented in figure 4(*d*) for the different gas boundary layer velocity profiles represented in figure 4(*c*) and characterized by their respective thickness δ defined conventionally as $\bar{u}_g(\bar{r} = \bar{f}(1+\delta)) = 0.99U_{g\infty}$; notice from (3.4) that for fixed Δ, the thickness δ depends only on the free parameter ζ_0. As expected, the jet radius decreases slower for thicker boundary layers. The downstream evolution of both the liquid and gas velocity profiles is represented in figures 5(*a*) and 5(*b*) for the cases $\Delta = 0.1$ and $\delta = 0.15$ which, as will be seen shortly, fit well the experimental observations. Notice in these figures the growth of the gas boundary layer and the acceleration of the liquid due to the transfer of axial momentum from the gas towards the liquid; observe that after few diameters downstream of $z = 0$ viscous diffusion renders the liquid velocity

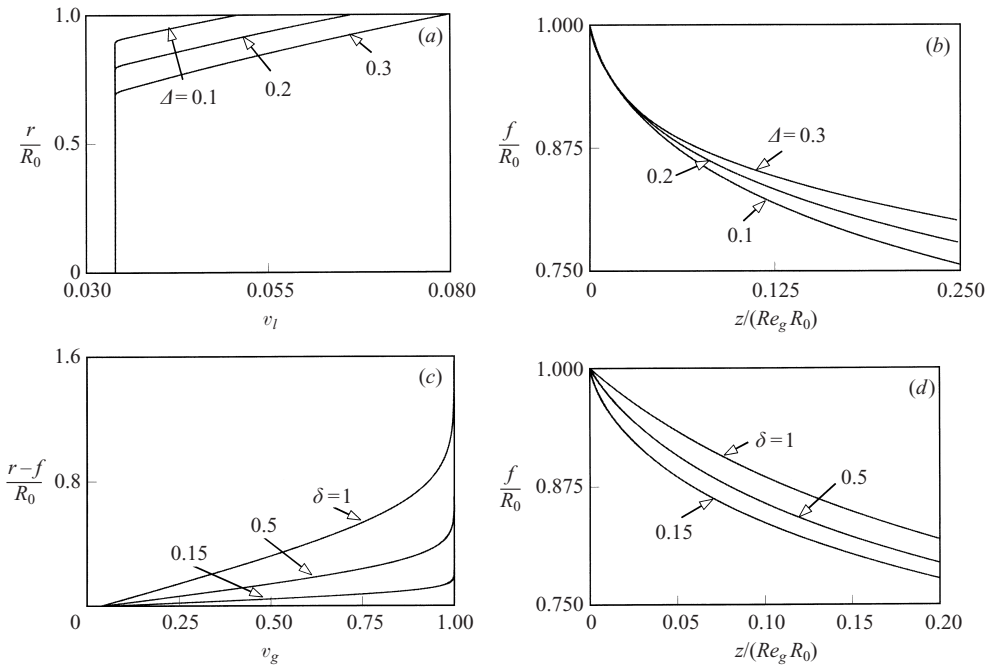

FIGURE 4. (*a*) Initial velocity profiles for the liquid jet; (*b*) downstream evolution of liquid jet radius for the initial conditions given in (*a*) and $\delta = 0.15$; (*c*) initial velocity profiles for the gas stream; (*d*) evolution of the liquid radius for the initial conditions given in (*c*) and $\Delta = 0.1$.

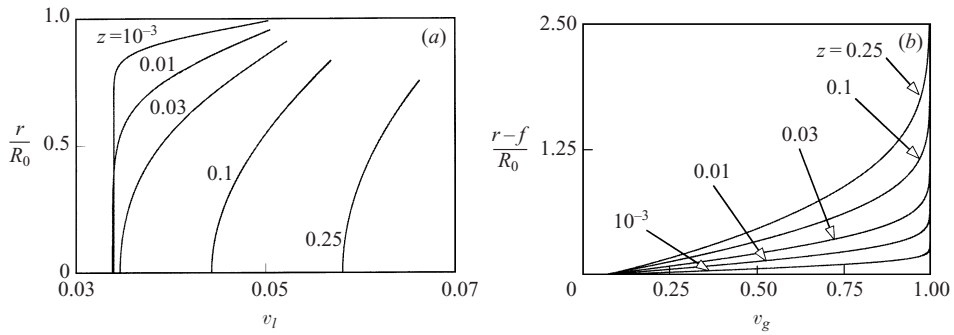

FIGURE 5. (*a*) Evolution of the liquid jet velocity profiles for $\delta = 0.15$ and $\Delta = 0.1$; (*b*) evolution of the gas velocity profiles for the same initial conditions as in (*a*).

profiles parabolic. Other quantities of interest such as the tangential stress and the velocity on the jet surface are represented in figure 6.

3.1. *Experimental setup and comparison with numerical results*

In order to determine the initial velocity profiles from experiments, we will perform measurements of the downstream evolution of the jet radius for different pressure drops between the chamber and the atmosphere and different water flow rates. The liquid jet shape is captured using a CCD camera connected to a microscope at the maximum magnification, in order to get the best resolution for the jet radius. Since the whole undisturbed jet length cannot be present in the same image, the atomizer is placed in a micro-positioner with a precision of 0.1 μm in order to equalize the

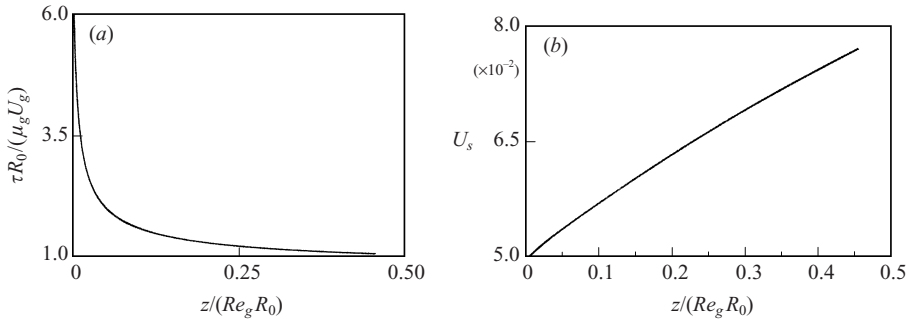

FIGURE 6. Downstream evolution of (*a*) the shear stress at the liquid surface; (*b*) the free surface velocity.

total liquid jet length from consecutive images and to measure distances in a very precise way. The next step is to measure the number of pixels of the liquid jet, and for this purpose the images have been processed, fixing a threshold grey level beyond which all the greys are considered as black and below which all greys are considered as white. Saving these images in a proper Post Script format it is easy to measure the number of pixels of the liquid jet at each axial station. Once the images are superposed a liquid jet shape like the one in figure 7 is obtained. Since our purpose is to compare with numerical results, an hyperbolic fit of fourth order is performed to all the images like that in figure 7. Figure 8(*a*) shows the numerical and experimental solution of the jet radius for a pressure drop of 10 KPa and for different flow rates Q. For each Q and for a given pressure drop (which determines u_c) the parameter Δ has been adjusted in such a way that (3.1)–(3.2) provide the required Q. Solid lines in figure 8(*a*) show the evolution of the jet shape for two pairs of values (Δ, ζ_0) – or which is the same (Δ, δ_0) – with Δ adjusted by the flow rate requirement in each case as explained above. Figure 8(*b*) shows the evolutions of the experimental and numerical results for a different pressure drop, namely 20 KPa; observe that the agreement is much better than in figure 8(*a*), in particular the experimental $Q = 30\,\mathrm{ml\,h^{-1}}$ is very well reproduced numerically for values of $\Delta = 0.15$ and $\delta_0 = 0.5$. The error in the measurements can be related mainly to the facts that: (i) in spite of using the microscope the liquid jet radius contains a limited number of pixels (50–100) and the resolution maybe not high enough, (ii) the smallness of the liquid jets ($\sim$ 30–60 μm) makes it difficult to focus the images, (iii) the fixed grey level introduce errors in the liquid radius. Nevertheless, since our main objective is to obtain an estimation of the parameters determining the initial conditions for the liquid and the gas streams which allows us to compute a realistic downstream evolution, we consider that the above procedure is able to provide us with the required information.

4. Stability analysis

Once the basic velocity profiles have been computed, we will analyse the stability of the equilibrium solutions obtained. In an initial approach to the problem, and in order to keep matters simple while still retaining the relevant physical phenomena, we have performed a standard temporal, inviscid stability analysis of locally parallel streams. Although it is known that the exact solution of the linear signalling problem leads, in general, to the study of spatial eigenvalues (Huerre & Monkewitz 1985), our approach can be justified if one takes into account that the temporal and spatial analysis yield

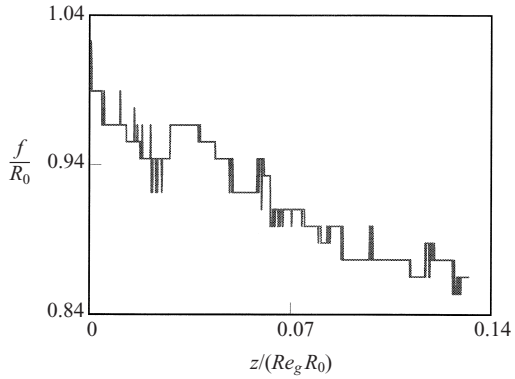

FIGURE 7. Radius of the jet before being fitted with a fourth-order hyperbolic regression.

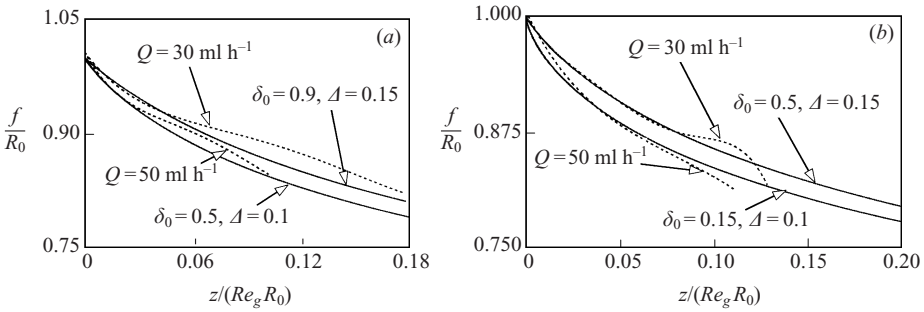

FIGURE 8. Jet radius profiles obtained numerically for: (*a*) $(\delta_0, \Delta) = (0.9, 0.15)$ and $(\delta_0, \Delta) = (0.5, 0.1)$ (continuous lines) and experimental profiles (dashed lines) for $Q = 30,\ 50\,\mathrm{ml\,h^{-1}}$ and $\Delta p = 10\,\mathrm{KPa}$ ($U_l = 4.5\,\mathrm{m\,s^{-1}}$ and $U_g = 127\,\mathrm{m\,s^{-1}}$); (*b*) $(\delta_0, \Delta) = (0.5, 0.15)$, $(\delta_0, \Delta) = (0.15, 0.1)$, $Q = 30,\ 50\,\mathrm{ml\,h^{-1}}$ and $\Delta p = 20\,\mathrm{KPa}$. ($U_l = 6.3\,\mathrm{m\,s^{-1}}$ and $U_g = 173\,\mathrm{m\,s^{-1}}$).

almost identical results for the growth rate and frequency of the perturbations (Li 1995). The assumption of inviscid perturbations demands that $\omega\lambda^2/\nu_g \gg 1$, where ω and λ are the typical frequency and wavelength of the perturbation and ν_g the gas kinematic viscosity (note that generally $\nu_l < \nu_g$ for liquid with viscosities close to that of water); as will be shown later, this parameter ($\omega\lambda^2/\nu_g$) turns out to be of the order of 10 in our analysis. The assumption of locally parallel streams requires that the typical axial distance for variations of the basic velocity profiles be much larger than the wavelength of the perturbation ($\lambda/U_\infty \partial U_g/\partial z \ll 1$); this hypothesis, to be confirmed later, allows us to consider the variable z as a parameter characterizing the values of the basic flow in the perturbation equations. Also, since the stability analysis is temporal, we will take advantage of the fact that the results will not change if the perturbation equations are expressed in a Galilean reference frame moving with the jet surface velocity at the given local z-station; in this frame the basic profiles used in the stability analysis are sketched in figure 9.

As usual, we decompose both liquid and gas velocities and pressures into this basic part and a perturbation

$$p = p_0(z) + \hat{p}(r, \theta, z, t), \quad R = R_0(z) + \hat{R}(\theta, z, t), \quad \boldsymbol{u}(r, \theta, z, t) = (\bar{U}_0(r) + \hat{u}, \hat{v}, \hat{w}), \quad (4.1)$$

where $\bar{U}_0$, R_0 and p_0 are the undisturbed velocity distribution, jet radius and pressure at station z respectively; $\hat{u}, \hat{v}, \hat{w}$ are the perturbed axial, radial and azimuthal velocity

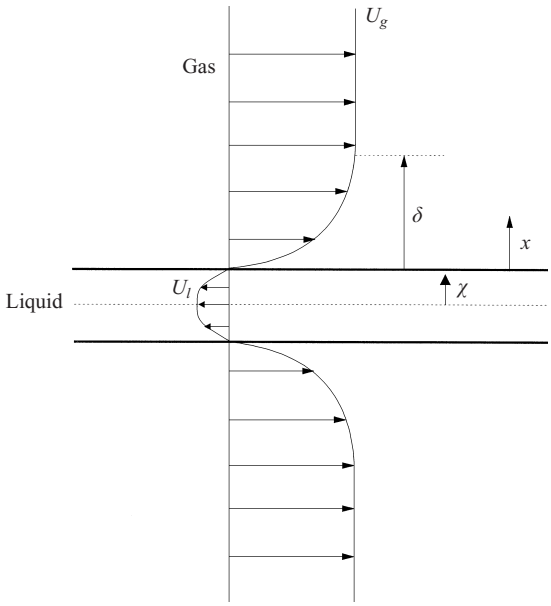

FIGURE 9. Sketch of the velocity profiles and variables used in the stability analysis at a generic downstream station.

components respectively and $\hat{p}$ and $\hat{R}$ the perturbed pressure and jet radius. Quantities referring to the gas (liquid) stream will be denoted with the subscript gl. Note that z is an independent variable for the perturbation, while U_0 and R_0, as usual, are considered to depend parametrically on the axial distance.

The equations governing the perturbed quantities defined in (4.1), can be obtained from the linearized Navier–Stokes equations as

$$\nabla \cdot \hat{\boldsymbol{u}} = 0, \tag{4.2}$$

$$-\frac{1}{\rho}\nabla^2 \hat{p} = 2\frac{\mathrm{d}\hat{U}_0}{\mathrm{d}r}\frac{\partial \hat{v}}{\partial z}, \tag{4.3}$$

$$\frac{\partial \hat{v}}{\partial t} + \hat{U}_0\frac{\partial \hat{v}}{\partial z} = -\frac{1}{\rho}\frac{\partial \hat{p}}{\partial r}, \tag{4.4}$$

$$\frac{\partial \hat{w}}{\partial t} + \hat{U}_0\frac{\partial \hat{w}}{\partial z} = -\frac{1}{\rho r}\frac{\partial \hat{p}}{\partial \theta}, \tag{4.5}$$

where, for convenience, the axial momentum equation has been replaced by the divergence of the momentum equation. Equations (4.2)–(4.5), of which there are two sets, one for the liquid and one for the gas, must be solved subject to regularity boundary conditions at the axis and at infinity:

$$r = 0: \quad \hat{\boldsymbol{u}}_l \neq \infty, \quad \hat{p}_l \neq \infty, \tag{4.6}$$

$$r \to \infty: \quad \hat{\boldsymbol{u}}_g \to 0, \quad \hat{p}_g \to 0, \tag{4.7}$$

together with the linearized free surface boundary conditions

$$r = R_0(z): \quad \hat{p}_l - \hat{p}_g = -\sigma\left(\frac{\hat{R}}{R_0^2} + \frac{\partial^2 \hat{R}}{\partial z^2} + \frac{\partial^2 \hat{R}}{R_0^2 \partial \theta^2}\right), \tag{4.8}$$

$$\hat{v}_l = \hat{v}_g = \frac{\partial \hat{R}}{\partial t}. \tag{4.9}$$

We shall look for solutions of (4.2)–(4.9) of the form

$$(\hat{u}, \hat{v}, \hat{w}, \hat{p}, \hat{R}) = (\bar{u}(r), \bar{v}(r), \bar{w}(r), \bar{p}(r), \bar{R}) \exp(\mathrm{i}(\bar{k}z - \bar{\Omega}t + m\theta)), \tag{4.10}$$

which when introduced into (4.3), and after eliminating $\bar{v}(r)$ using (4.4), provide the equation for the gas pressure

$$\frac{1}{r}\frac{\mathrm{d}}{\mathrm{d}r}(r\frac{\mathrm{d}\bar{p}_g}{\mathrm{d}r}) - 2\frac{\bar{k}}{(\bar{U}_{0g}\bar{k} - \bar{\Omega})}\frac{\mathrm{d}\bar{U}_{0g}}{\mathrm{d}r}\frac{\mathrm{d}\bar{p}_g}{\mathrm{d}r} - \left(\bar{k}^2 + \frac{m^2}{r^2}\right)\bar{p}_g = 0, \tag{4.11}$$

and, analogously, the equation for the liquid pressure

$$\frac{1}{r}\frac{\mathrm{d}}{\mathrm{d}r}\left(r\frac{\mathrm{d}\bar{p}_l}{\mathrm{d}r}\right) - 2\frac{\bar{k}}{(\bar{U}_{0l}\bar{k} - \bar{\Omega})}\frac{\mathrm{d}\bar{U}_{0l}}{\mathrm{d}r}\frac{\mathrm{d}\bar{p}_l}{\mathrm{d}r} - \left(\bar{k}^2 + \frac{m^2}{r^2}\right)\bar{p}_l = 0. \tag{4.12}$$

The boundary conditions (4.8)–(4.9) can be expressed in terms of the gas and liquid pressures using the radial momentum equation (4.4) as

$$\bar{p}_l = \bar{p}_g - \frac{\sigma}{{R_0}^2}(1 - k^2{R_0}^2 - m^2)\frac{1}{\rho_g\bar{\Omega}^2}\frac{\mathrm{d}\bar{p}_g}{\mathrm{d}r}, \tag{4.13}$$

$$\frac{\mathrm{d}\bar{p}_l}{\mathrm{d}r} = \frac{\rho_l}{\rho_g}\frac{\mathrm{d}\bar{p}_g}{\mathrm{d}r}. \tag{4.14}$$

In terms of the dimensionless parameters and variables

$$M = \frac{\rho_l}{\rho_g}, \quad We = \frac{\rho_g {U_\infty}^2 R_0}{\sigma}, \quad \kappa = \bar{k}R_0, \tag{4.15}$$

$$x = \frac{r - R_0}{R_0\delta(z)}, \quad p = \frac{\bar{p}}{\rho_g {U^2}_\infty}, \quad \omega = \frac{\bar{\Omega}}{\bar{k}U_\infty}, \quad U(r) = \frac{\bar{U}_0(r)}{U_\infty}, \quad \chi = \frac{r}{R_0}, \tag{4.16}$$

equations (4.11)–(4.12) and boundary conditions (4.6)–(4.7) and (4.13)–(4.14) for the perturbed pressures can be written as

$$\frac{\mathrm{d}^2 p_g}{\mathrm{d}x^2} + \left(\frac{\delta}{1 + \delta x} - \frac{2}{U_g - \omega}\frac{\mathrm{d}U_g}{\mathrm{d}x}\right)\frac{\mathrm{d}p_g}{\mathrm{d}x} - \left(\kappa^2\delta^2 + \frac{m^2\delta^2}{(1 + \delta x)^2}\right)p_g = 0, \tag{4.17}$$

$$\frac{\mathrm{d}^2 p_l}{\mathrm{d}\chi^2} + \left(\frac{1}{\chi} - \frac{2}{U_l - \omega}\frac{\mathrm{d}U_l}{\mathrm{d}\chi}\right)\frac{\mathrm{d}p_l}{\mathrm{d}\chi} - \left(\kappa^2 + \frac{m^2}{\chi^2}\right)p_l = 0, \tag{4.18}$$

$$x = 0, \quad \chi = 1: \quad \kappa^2\omega^2\left(M\frac{p_l(1)}{\mathrm{d}p_l/\mathrm{d}\chi(1)} - \delta\frac{p_g(0)}{\mathrm{d}p_g/\mathrm{d}x(0)}\right) + We^{-1}(1 - \kappa^2 - m^2) = 0, \tag{4.19}$$

$$x \to \infty: \quad p_g \to 0, \quad \chi = 0, \quad p_l \quad \text{finite}, \tag{4.20}$$

where condition (4.19), which has been obtained by dividing (4.13) by (4.14), eliminates free constants due to the linearity of the problem. The parameter We in (4.19) is the well-known Weber number, which is the ratio of the dynamical to capillary pressures. Notice that this parameter is based on the velocity relative to the moving frame $U_\infty(z)$ of the gas stream at infinity and on the unperturbed radius of the jet $R_0(z)$. The parameter $\delta(z)$ is the dimensionless gas boundary layer thickness of the equilibrium problem defined in § 3. The problem (4.17)–(4.20) does not have non-trivial solutions

except for certain complex values of ω which satisfy the dispersion relation (4.19) for given real values of κ, We and M. The dispersion relation also contains $p_l(1)/\mathrm{d}p_l/\mathrm{d}\chi(1)$ and $p_g(0)/\mathrm{d}p_g/\mathrm{d}x(0)$ which in turn are determined through integration of (4.17)–(4.18) subject to the boundary conditions (4.20). To obtain $p_l(\chi)$, equation (4.18) has been integrated numerically from $\chi = \chi_0 \ll 1$ (to avoid the singularity at $\chi = 0$) up to $\chi = 1$ using starting values provided by the Frobenius method (Arfken & Weber 1995), namely

$$p_l = 1 + {\chi_0}^2 \frac{\kappa^2}{4}, \quad \frac{\mathrm{d}p_l}{\mathrm{d}\chi} = \chi_0 \frac{\kappa^2}{2} \quad \text{if} \quad m = 0, \tag{4.21}$$

$$p_l = {\chi_0}^m, \quad \frac{\mathrm{d}p_l}{\mathrm{d}\chi} = m{\chi_0}^{m-1} \quad \text{if} \quad m \neq 0. \tag{4.22}$$

To obtain $p_g(x)$ we integrate equation (4.17) from $x = 0$ to $x = \infty$ taking into account that, except for $p_g(0)$ and $\mathrm{d}p_g/\mathrm{d}x(0)$ which should be known 'exactly', the numerical solution will unavoidably tend to the modified Bessel function of the first kind, $I_m[\kappa(1+\delta x)]$, which is the equation's attractor at infinity, and thus will not satisfy the boundary conditions at infinity. Nevertheless, due to a well-known result of the theory of second-order linear ODEs (Arfken & Weber 1995), given any particular solution $n(x)$, obtained for example by integrating (4.17) from $x = 0$ with initial conditions

$$n(0) = 1, \quad \frac{\mathrm{d}n}{\mathrm{d}x}(0) = 0, \tag{4.23}$$

another independent solution of (4.17) can be constructed numerically from $n(x)$ in the form

$$p_g(x) = n(x) \int_\infty^x \frac{\exp\left(-\int_0^z \left(\dfrac{\delta}{\delta s + 1} - \dfrac{2\mathrm{d}U_g/\mathrm{d}s}{U_g - \omega}\right) \mathrm{d}s\right)}{n(z)^2} \mathrm{d}z\,. \tag{4.24}$$

Since $n(x \to \infty) \to \infty$ it is clear that $p_g(x \to \infty) \to 0$. At $x = 0$, (4.24) yields

$$\frac{p_g(0)}{\mathrm{d}p_g/\mathrm{d}x(0)} = -\frac{1}{\omega^2} \int_0^\infty \frac{(U_g - \omega)^2}{n(x)^2(1 + \delta x)} \mathrm{d}x. \tag{4.25}$$

5. Numerical results

It is our objective in this section to show that the stability analysis of our simplified basic model described above is able to explain the appearance of the different atomization regimes observed in our experiments and to shed light on the physical mechanisms that lead to the appearance of different instability modes. Therefore, before considering the general case (that will be studied extensively in § 5.3), in which the spectrum of eigenvalues is worked out numerically using the basic velocity profiles of § 3, and in order to learn what is the specific role of the basic velocity profiles of either the liquid or the gas, two simplified models, A and B, will be solved first.

Model A: a liquid jet of constant radius and uniform velocity profile surrounded by a coaxial gas stream where the velocity profile is computed numerically as described in § 2. In this model, both Rayleigh and Taylor atomization regimes are identified. In the Rayleigh regime, the breakup wavelengths are of the order of the jet radius and the instability is promoted by surface tension, whereas in the Taylor regime the wavelengths of the disturbances are much smaller than the jet radius and the instability mechanism is the work done by the gas pressure fluctuations over the liquid surface in the absence of viscosity in the stability analysis (Lin & Chen 1998).

These breakup regimes are found for different ranges of the value of the only free parameter, δ (gas boundary layer thickness), since We and M are kept constant. Besides, a new type of helicoidal mode (the first non-axisymmetric or sinuous†) is found. Model A is merely an extension to a cylindrical geometry of the model used in Villermaux (1998) which, in spite of being able to predict the breakup frequencies measured in their experiments, is unable to explain the different breakup features present in ours. This is due to the fact that in our case the gas-to-liquid momentum ratio ($M_r = \rho_g {U_g}^2/\rho_l {U_l}^2$) is very close to unity, which makes the role of the basic liquid velocity profile (specifically the liquid shear layer) essential in explaining the appearance of the modes that lead to the jet breakup, the gas shear layer being merely a source of energy for these perturbations to grow faster. This role of the liquid shear layer is clearly shown in the model described next.

Model B: coflowing liquid and gas streams, where basic velocity profiles have been computed in § 3, but perturbations are introduced only in the liquid jet assuming that the gas stream remains unperturbed. The interest of this case lies in the fact that a non-uniform liquid velocity profile modifies Rayleigh's results substantially, and new modes appear associated with the existence of a boundary layer near the liquid surface; to the best of our knowledge these modes have not been explored previously in the literature.

5.1. *Model A: stability of a liquid jet of constant radius with uniform velocity profile surrounded by a coaxial gas stream*

The basic solution for this problem obtained with the method of lines described in § 2 is represented in figure 10, and compares well with the asymptotic results given by Glauert and Lighthill (Rosenhead 1963) for the same problem. As shown in the figure, velocity profiles with $\delta \lesssim 0.1$ approach closely those of a Blasius boundary layer, while for larger δ curvature effects become important and the profiles differ from the Blasius ones. Figure 11(a, b) represent the real and imaginary parts respectively of the dimensionless eigenfrequencies $\Omega = \omega\kappa = \bar{\Omega} R_0/U_\infty$ versus the dimensionless wavenumber $\kappa = \bar{k} R_0$ of the unstable axisymmetric ($m = 0$) modes for basic velocity profiles characterized by small dimensionless boundary layer thicknesses δ. Notice that, as δ and κ increase the unstable modes are excited at ever larger frequencies Ω_r – see figure 11(a). However, the behaviour with δ of the temporal growth rate Ω_i is more complicated. In effect, as figure 11(b) shows, the area under the curves Ω versus κ first increases dramatically from $\delta = 0$ up to $\delta = 0.001$, and then decreases monotonically with increasing δ. The values corresponding to the Kelvin–Helmholtz (K–H) model lie on the curve labelled as $\delta = 0$ in figure 11(b). Observe that, although $\delta \ll 1$ in figure 11(b), the Kelvin–Helmholtz results are not reproduced in the whole range of wavelengths except for the smallest values of δ ($\delta = 10^{-5}$). Basic velocity profiles with larger δ give growth rates that deviate substantially from the K–H model at short wavelengths: they are larger for $0 < \delta \leqslant 0.015$ and lower for $\delta \geqslant 0.015$, while all velocity profiles give growth rates similar to the K–H ones at large wavelengths. This fact suggests that, even for small thicknesses, the structure of the boundary layer plays a crucial role in the development of the instability of perturbations of short wavelengths due perhaps to the existence of a critical layer (Miles 1957) located at a radius such that $U_g \kappa \simeq \Omega_r$ where the transfer of energy between the basic flow and

† The first non-axisymmetric mode ($m = 1$) is usually termed sinuous mode in the literature. However, we have named them helicoidal since the dependence on z and θ of the eigenfunctions make the radius of the jet of the form $R = R_0 + R\cos(kz + \theta)$ for $m = 1$. A planar, sinuous structure can be recovered if we add modes with $m = \pm 1$.

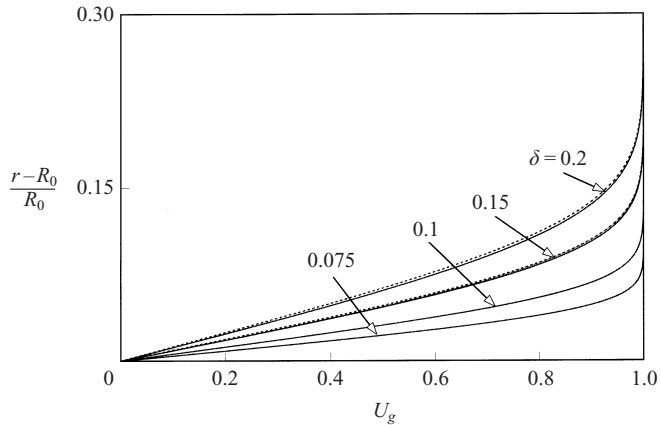

FIGURE 10. Computed basic gas velocity profiles for model A (dashed lines) and the Blasius profile (continuous line).

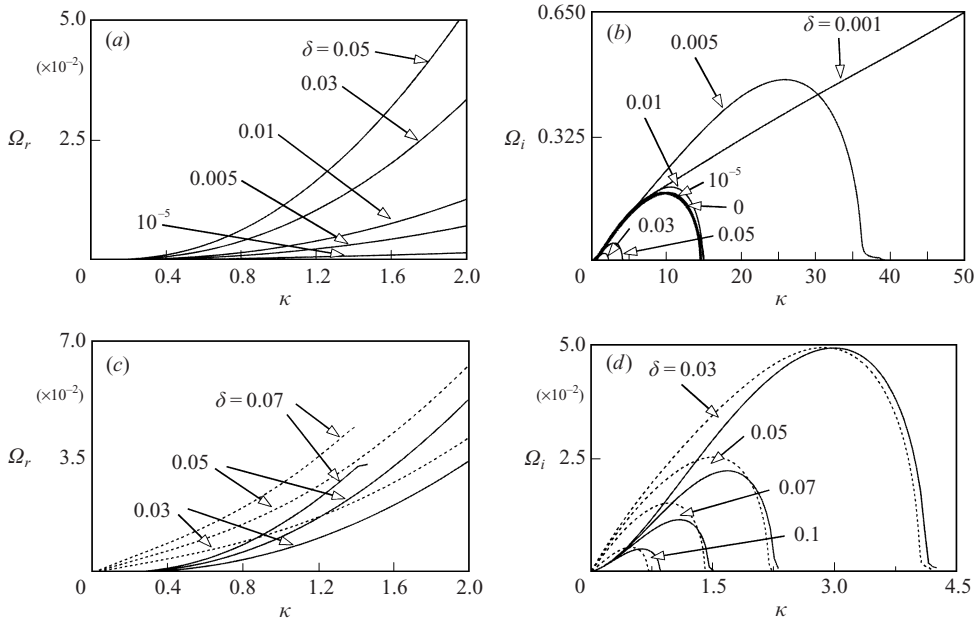

FIGURE 11. (*a*) Real and (*b*) imaginary eigenfrequencies of axisymmetric modes for different values of δ; (*c*) real and (*d*) imaginary eigenfrequencies of the axisymmetric (continuous lines) and the helicoidal modes (dashed lines) for different values of δ; $We = 15$ and $M = 850$.

the perturbation modifies substantially the dynamical effects involved in the K–H mechanism. Figures 11(*c*) and 11(*d*) shows Ω_r and Ω_i as functions of κ for unstable axisymmetric (continuous lines) and helicoidal ($m = 1$) modes obtained with basic velocity profiles of small δ; only results for $\delta > 0.01$ are presented since for smaller δ the growth rates of helicoidal and axisymmetric modes turn out to be very similar. Notice in figure 11(*d*) that helicoidal disturbances grow faster than axisymmetric ones for larger wavelengths while the opposite occurs for shorter wavelengths (Yang 1992).

The boundary layer thicknesses required for the validity of the results discussed in the above paragraph are so small compared to the liquid jet radius that this might

be far from realistic in some practical situations, as is the case in our atomization experiments. In effect, δ decreases with increasing $Re = U_\infty R_0/\nu_g$, which for typical atomization experiments with $D_0 \sim 50\,\mu\text{m}$ and $U_\infty \sim 100\,\text{m}\,\text{s}^{-1}$ is of the order of $Re \sim 500$, a value which is probably too low to very small δ. This is supported by the experimental results shown in figure 8(a, b) which suggest values of δ larger than 0.1. Therefore we will consider now the case in which the boundary layer thickness is of the order of the jet radius, $\delta \sim O(1)$. We have performed the stability analysis for three different basic velocity profiles computed at the stations $z = 0.01$, 0.05 and 0.1 for which the corresponding values of δ are $\delta = 0.46$, 0.98 and 1.35 respectively. Observe that the parallel flow condition is met for these values since we can estimate from them $(\lambda/\bar{\delta})\mathrm{d}\bar{\delta}/\mathrm{d}\bar{z} = \lambda/(\delta R_0 Re)\mathrm{d}\delta/\mathrm{d}z \sim 0.1$, where $\bar{\delta} = \delta R_0$, $\bar{z} = R_0\,Re\,z$ are the dimensional boundary layer thickness and axial distance. In these cases we have found one family of unstable axisymmetric modes ($m = 0$) and two families of unstable helicoidal modes ($m = 1$) with very different frequencies and growth rates. Figure 12(a, b) shows the frequencies and growth rates of the axisymmetric modes (continuous lines) and one family of helicoidal modes (dashed line) whose excitation frequencies are of the order of the dimensionless capillary frequency $\Omega_r \sim (MWe)^{-1/2}$ for the values of $We = 15$ and $M = 850$ considered in this calculation. Observe in figure 12(b) that the growth rates of the helicoidal modes are much less than those of the axisymmetric modes, and that the latter nearly coincide for all values of κ with those corresponding to the Rayleigh model. Both facts indicate that the boundary layer is so thick that the dynamics of the gas stream has no influence on the instability mechanism of the liquid jet, being the capillary effects responsible for the breakup process. The frequencies and growth rates of the second family of unstable helicoidal modes are represented in figure 13(a, b). Observe that their excitation frequencies, of the order $\Omega \sim O(1)$, are much larger than the capillary one, which indicates that these modes have an hydrodynamic nature and will be called *wake modes* since they are analogous to the ones found by Batchelor & Gill (1962) for the stability of a far-field jet (notice that, since their stability analysis is temporal, Batchelor & Gill's results are not modified if a negative uniform velocity profile is added to the far-field jet profile, which in turn is transformed in a wake velocity profile). As figure 13(b) shows, the growth rates for the wake modes are of same order of magnitude as the growth rates of the axisymmetric modes, but their group velocity is of order $c_g/U_\infty = \mathrm{d}\Omega_r/\mathrm{d}\kappa \sim 0.3$ as estimated from figure 13(a), about twenty times larger than that of the axisymmetric modes as estimated from figure 12(a). Thus the wake modes travel so fast downstream along the liquid jet that they have no time to grow as much as the capillary axisymmetric modes before leaving the jet, and therefore model A is unable to predict the helicoidal breakdown of the liquid jet observed in atomization experiments for sufficiently high Weber numbers.

5.2. *Model B: stability of a liquid jet with no uniform velocity profile surrounded by an unperturbed coaxial gas stream*

In this simplified model, as well as in the next one, the liquid and gas basic velocity profiles are the ones corresponding to figure 8(b) in the case of $\delta_0 = 0.5$ and $\Delta = 0.15$†. However, in the stability analysis we have introduced perturbations only in the liquid jet and held the gas stream unperturbed. We have found two families of axisymmetric

† Note that in the following, z is a parameter that determines the basic velocity profiles used in the stability analysis.

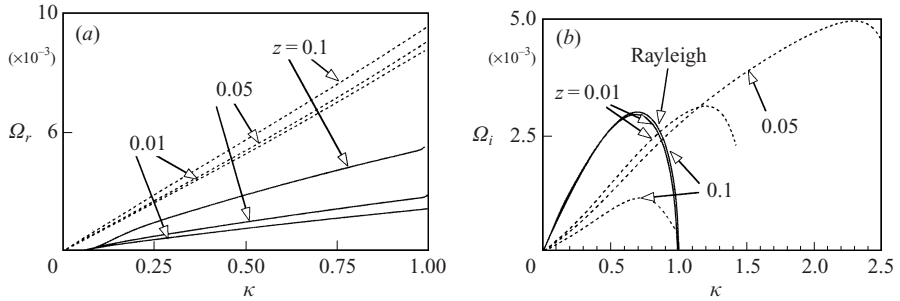

FIGURE 12. (*a*) Real and (*b*) imaginary eigenfrequencies at different z stations of axisymmetric (continuous lines) and helicoidal modes (the helicoidal growth rates are multiplied by a factor of 100 in *b*). $We = 15$ and $M = 850$.

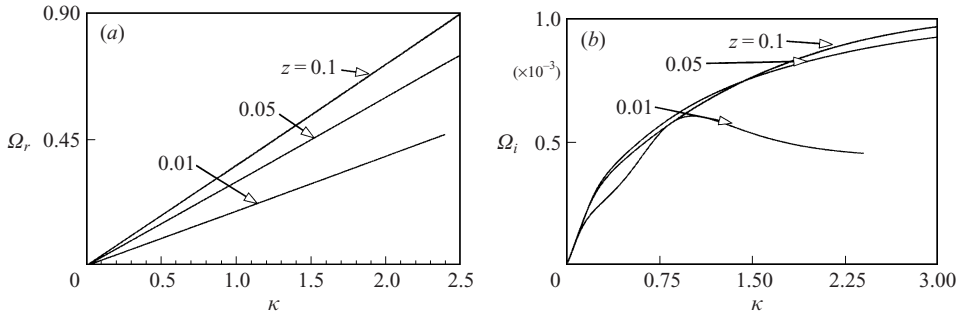

FIGURE 13. (*a*) Real and (*b*) imaginary eigenfrequencies for the wake modes. $We = 15$ and $M = 850$.

($m = 0$) unstable modes, and one family of helicoidal ($m = 1$) unstable modes which appears only at sufficiently high Weber numbers.

The frequencies and growth rate of the first family of unstable modes, of capillary type, are plotted in figure 14(*a*, *b*). Observe that the excitation frequencies increase with increasing κ, and that the growth rates tend to the Rayleigh limit as z increases (the liquid velocity profile relaxes and becomes more uniform). The attenuation of the growth rates with increasing non-uniformity of the liquid jet velocity profile is supported by the results found by Leib & Goldstein (1986) in their analysis of the Rayleigh problem with a basic parabolic velocity profile and later proved theoretically by Miyazaki & Kubo (1995) for a related problem. The second family of unstable modes is also of axisymmetric nature and their frequencies and growth rates are represented in figure 14(*c*, *d*). Observe that, contrary to the capillary modes, their growth rates decrease as the velocity profile flattens, and so this family will be called *axisymmetric hydrodynamic modes*, their existence being associated with radial velocity gradients in the bulk of the liquid jet and not to capillary forces. Notice that, although both capillary and axisymmetric hydrodynamic modes coexist, their growth rates are markedly different depending on the value of z. Finally, at sufficiently high Weber numbers a third family of unstable modes of helicoidal nature appear, their growth rates being represented in figure 14(*e*) where we compare them with those of the axisymmetric hydrodynamic modes at different Weber numbers. Observe that as We increases (the relative importance of surface tension decreases) the growth rates of the helicoidal modes increase and become similar to those of the axisymmetric hydrodynamic modes,

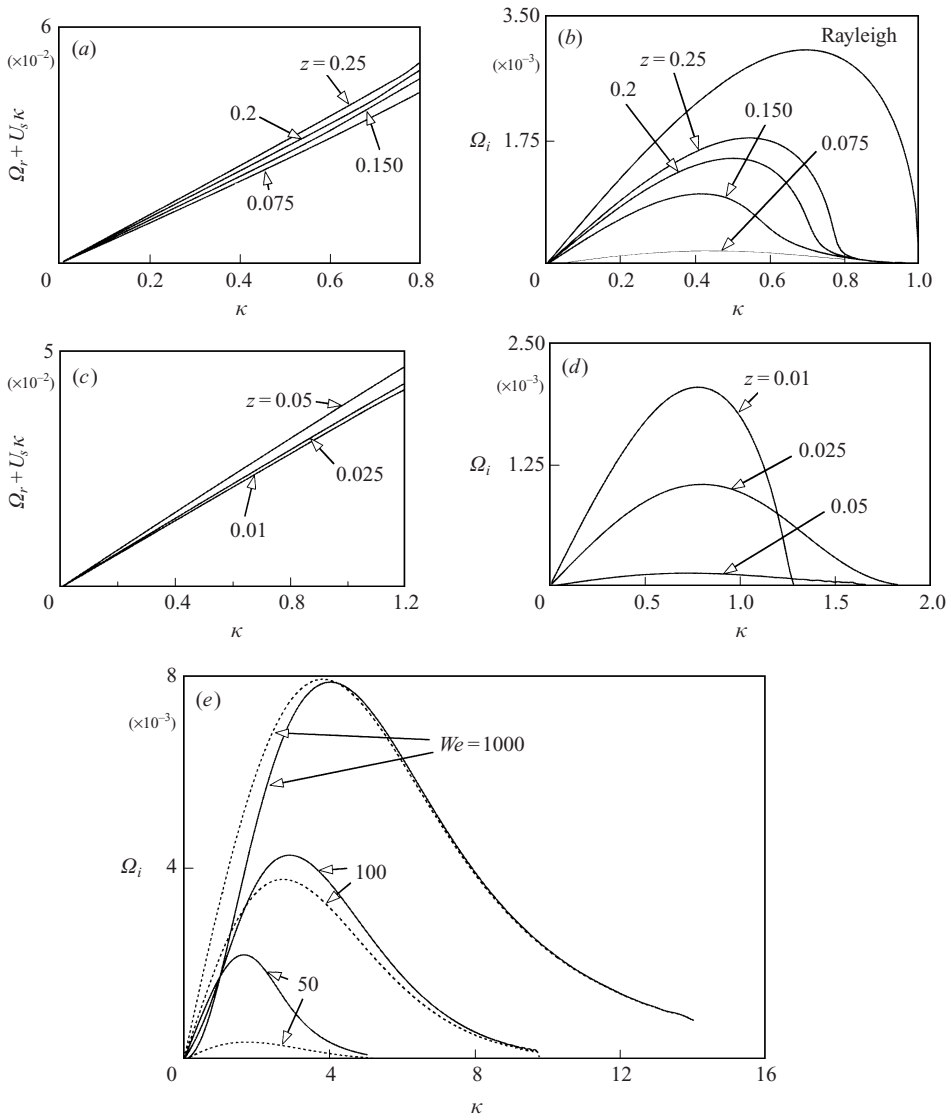

FIGURE 14. (*a*) Real and (*b*) imaginary eigenfrequencies of the axisymmetric capillary modes at different z stations; (*c*): real and (*d*) imaginary eigenfrequencies for the axisymmetric hydrodynamic modes at different z stations; (*e*) growth rates of the hydrodynamic and helicoidal modes for different Weber numbers at $z = 0.01$. Continuous lines represent axisymmetric modes. In (*a–d*) $We = 15$ and $M = 850$. U_s is the free surface velocity.

which indicates that the nature of the helicoidal modes is also hydrodynamic. However, as We decreases the differences between these two families sharpens, and it is seen in figure 14(*e*) that while there is a minimum value of We below which the helicoidal modes become stable, we have not found such a lower bound for the axisymmetric hydrodynamic modes. The difference of behaviour at low We can be explained on physical grounds if one takes into account that a high surface tension tends to inhibit the appearance of a helicoidal shape but may favour the instability of an axisymmetric shape. Therefore, using this model we have identi-

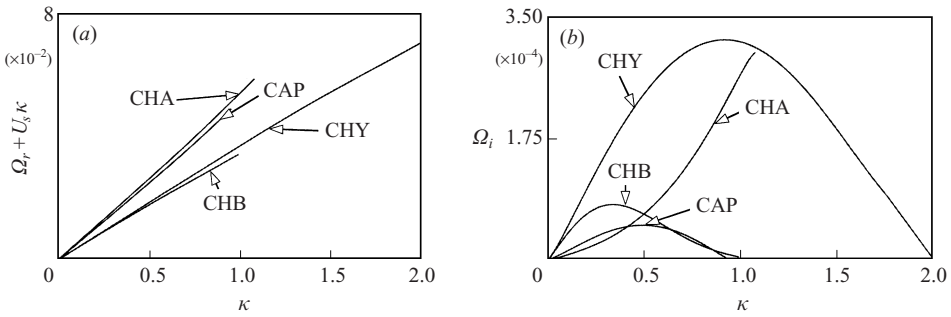

FIGURE 15. (*a*) Real and (*b*) imaginary eigenvalues of the different modes excited at frequencies of the order U_l/R_0 at the section $z = 0.025$ for $We = 15$ and $M = 850$ (the growth rates of the helicoidal modes of type A (CHA) are multiplied by a factor of 100, and the axisymmetric hydrodynamic ones (CHY) are divided by a factor of 5).

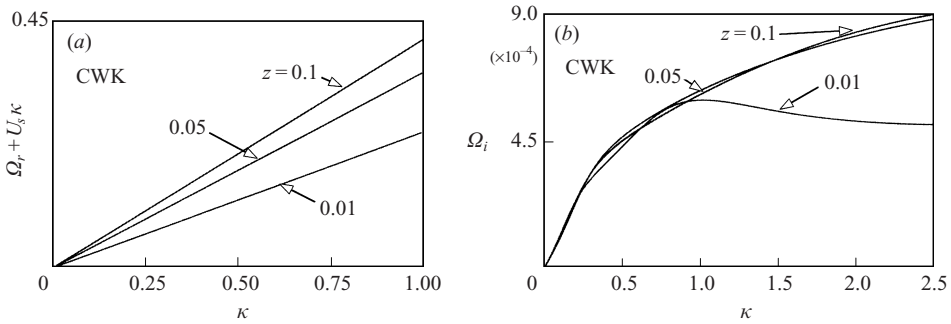

FIGURE 16. (*a*) Real and (*b*) imaginary eigenvalues of the wake modes for model C.

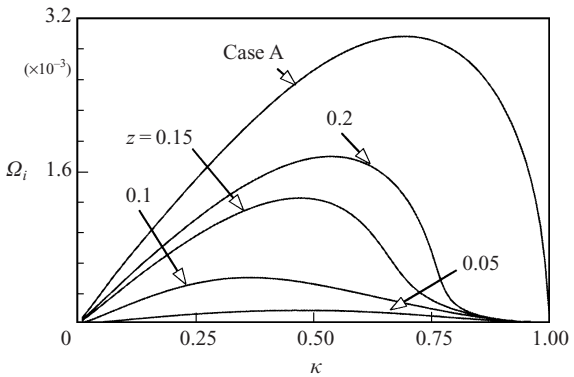

FIGURE 17. Growth rates of the capillary axisymmetric modes of model A and of model C at different z stations for $We = 15$ and $M = 850$.

fied two different kinds of modes that have a completely different nature to the ones (Rayleigh–Taylor) previously reported in the literature. The origin of these new modes is related to the existence of a strong shear layer in the liquid phase, and the effect of the perturbations in the gas is only to increase the growth rates of these modes due to the work of the gas pressure forces over the jet surface (Lin & Chen 1998).

5.3. *Model C: Stability of a liquid jet with no uniform velocity profile surrounded by a coaxial gas stream*

In this section we present the results of the stability analysis performed taking into account both liquid and gas velocity profiles, computed self-consistently in § 3, and introducing perturbations in both streams. Typical frequencies and growth rates of the modes which appear in this case are represented in figures 15 and 16. Figure 15(*a*) shows the growth rates for different types of modes whose frequencies are of the order of the capillary one (U_l/R_0). Within this group there are two axisymmetric modes (denoted by CAP and CHY) and two helicoidal modes (denoted by CHA and CHB). As will be seen shortly the modes CAP can be related to the capillary axisymmetric modes previously found in models A and B, the modes of the type CHY to the axisymmetric hydrodynamic modes of model B, and the modes CHA and CHB to the helicoidal modes of A and B respectively. The growth rates of these modes are represented in figure 15(*b*) (notice that the values corresponding to the modes CHA have been multiplied by a factor of 10^2, and the values corresponding to CHY have been divided by 5). Figure 16(*a*, *b*) shows the fifth family of modes found with model C, labelled CWK, whose frequencies and growth rates are of the order of the *wake modes* found in model A – see figure 13. It is of interest to analyse further the relation between the two simpler cases A and B and the more realistic model C. For instance, figure 17 shows the growth rates of capillary axisymmetric modes computed for basic velocity profiles at different z-stations, for the model A and for the model C (type CAP); observe that while model A yields Rayleigh's solution at all stations, the growth rates of model C are substantially lower, depend on the velocity profile, and approach Rayleigh's only in the limit $z \to \infty$. Although the modes CHA of figure 15 are clearly analogous to the helicoidal modes of model A – figure 12 – we will not consider them further owing to their small growth rates. The growth rates of the capillary axisymmetric modes for models B and C (type CAP) at different z-stations are shown in figure 18(*a*) where the larger values obtained for model C are attributed to the effect of the supply of energy that the perturbed gas pressure exerts over the jet surface which is absent in B. This effect can be also seen in figure 18(*b*) for modes of type CHY and the axisymmetric hydrodynamic modes of model B. Figure 18(*c*) is analogous to figure 14(*e*) and shows the behaviour with the Weber number of the hydrodynamic helicoidal modes of both model B and model C (type CHB); observe that, as pointed in § 5.2, there exists a minimum value of the Weber number below which the modes are stable, and the same happens for the CHB modes, although the cutoff Weber number is lower than in the case of model B. This must be attributed to the effect of the perturbations of the air stream which make the growth rates of the CHB modes higher than those of the model B modes, although the difference in growth rates gets lower as We increases.

Next we will analyse the behaviour of the modes of model C for variations of downstream distance z (flattening of the velocity profiles), the Weber number, We, and the liquid-to-gas density ratio M. Figure 19 shows the frequencies and growth rates of the modes CAP, CHY and CHB at different z stations. As the velocity profiles flatten the growth rates of the capillary axisymmetric modes (CAP) increase, which reflects the capillary nature of these modes, while the growth rates of the helicoidal and hydrodynamic (CHB and CHY) modes decrease, which reflects their hydrodynamic nature. Figure 20 shows the growth rates of the capillary axisymmetric, helicoidal and hydrodynamic modes for model C, for different Weber numbers and at a given station $z = 0.05$ (the helicoidal modes for $We = 10$ are not shown since their growth rates are negligible within the scale of the figure). The type of mode with

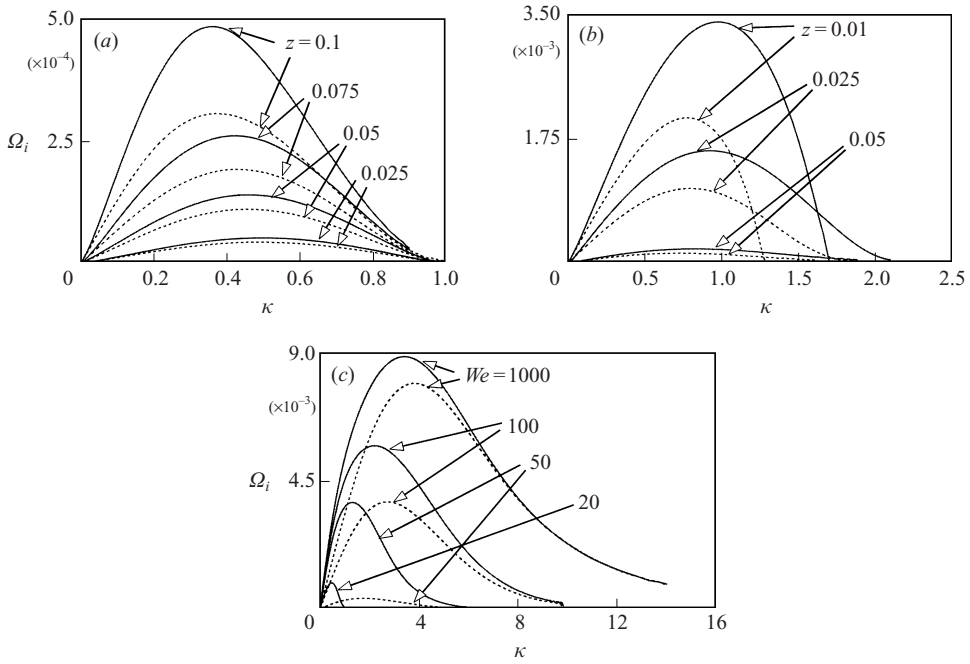

FIGURE 18. Growth rates of (*a*) the capillary axisymmetric (*b*) and hydrodynamic modes in the case of no external gas stream (dashed lines) and with external gas stream (continuous lines) at different z stations ($We = 15$ and $M = 850$); (*c*) growth rates of the helicoidal modes in the case of no external gas stream (dashed lines) and with external gas stream for different Weber numbers at the fixed station $z = 0.01$ and for $M = 850$.

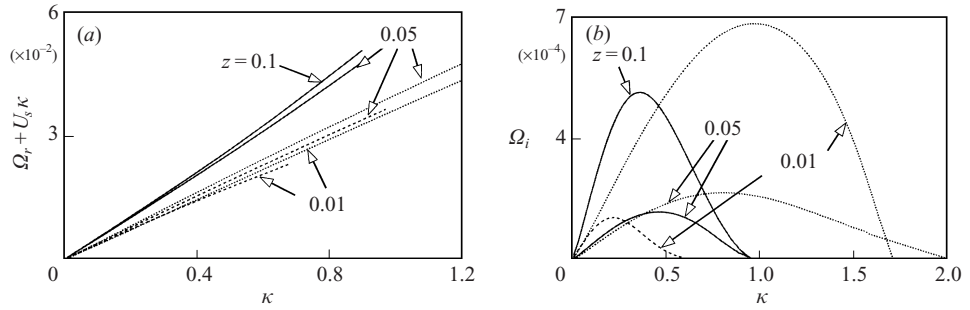

FIGURE 19. (*a*) Real and (*b*) imaginary eigenfrequencies of the axisymmetric capillary modes (continuous lines), helicoidal modes (dashed lines) and hydrodynamic axisymmetric modes (dots) at different z stations for $We = 15$ and $M = 850$. Note that the growth rates of the hydrodynamic axisymmetric modes in (*b*) have been divided by a factor of 5.

highest growth rates depends on the Weber number, that is, on the relative importance of surface tension: for instance, for $We = 10$ the capillary axisymmetric mode is the one with highest growth rates, for $We = 15$ it is the axisymmetric hydrodynamic mode, while for $We = 20$ the growth rates are highest for the helicoidal mode. Figure 21 shows the influence of the liquid-to-gas density ratio M and the growth rates of the CAP, CHB and CHY modes. As M increases the growth rates of the CAP and CHY modes decrease while those of CHB increase. This type of behaviour, which is expected for the capillary axisymmetric modes, reveals that the liquid inertia

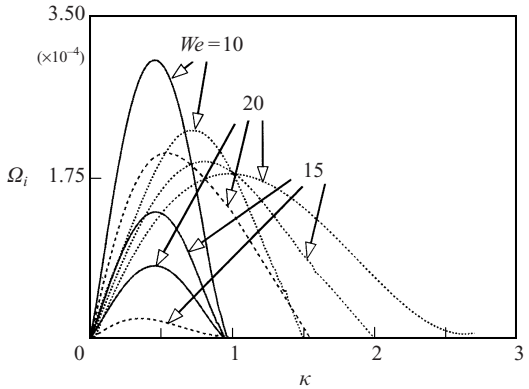

FIGURE 20. Growth rates of the axisymmetric capillary modes (continuous lines), helicoidal modes (dashed lines) and hydrodynamic axisymmetric modes (dots) for different Weber numbers at the station $z = 0.05$; $M = 850$.

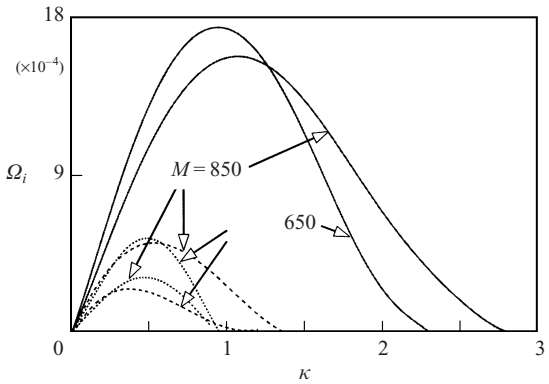

FIGURE 21. Growth rates of the axisymmetric capillary modes (dots), helicoidal modes (dashed lines) and hydrodynamic axisymmetric modes (continuous lines) for two values of M at the station $z = 0.025$ and for $We = 20$ (the growth rates of the capillary axisymmetric modes are multiplied by a factor of 10).

favours the development of hydrodynamic instabilities of helicoidal type instead of axisymmetric ones.

6. Comparison with experiments

In this section the numerical results discussed in § 5 are compared with those obtained in the series of atomization experiments shown in figure 22(*a–f*). The experiments have been performed with the atomization device sketched in figure 2(*a*) using a fixed flow rate of water of $Q = 30\,\mathrm{ml\,h^{-1}}$ and an increasing pressure difference, Δp, between the air in the chamber and the atmosphere. The images were captured using a CCD camera with a light intensifier which allows an exposure time as short as 10 ns. In figure 22, parts (*a–c*, *f*) show an axisymmetric breakup, while in (*d*) and (*e*) the jet breaks in a helicoidal mode. For the lowest Δp, corresponding to figure 22(*a*), the measured breakup wavelength is very close to Rayleigh's which indicates a capillary axisymmetric instability mechanism which can be explained if one takes into account that the velocity profiles flatten in both the gas and the liquid for decreasing Δp, giving

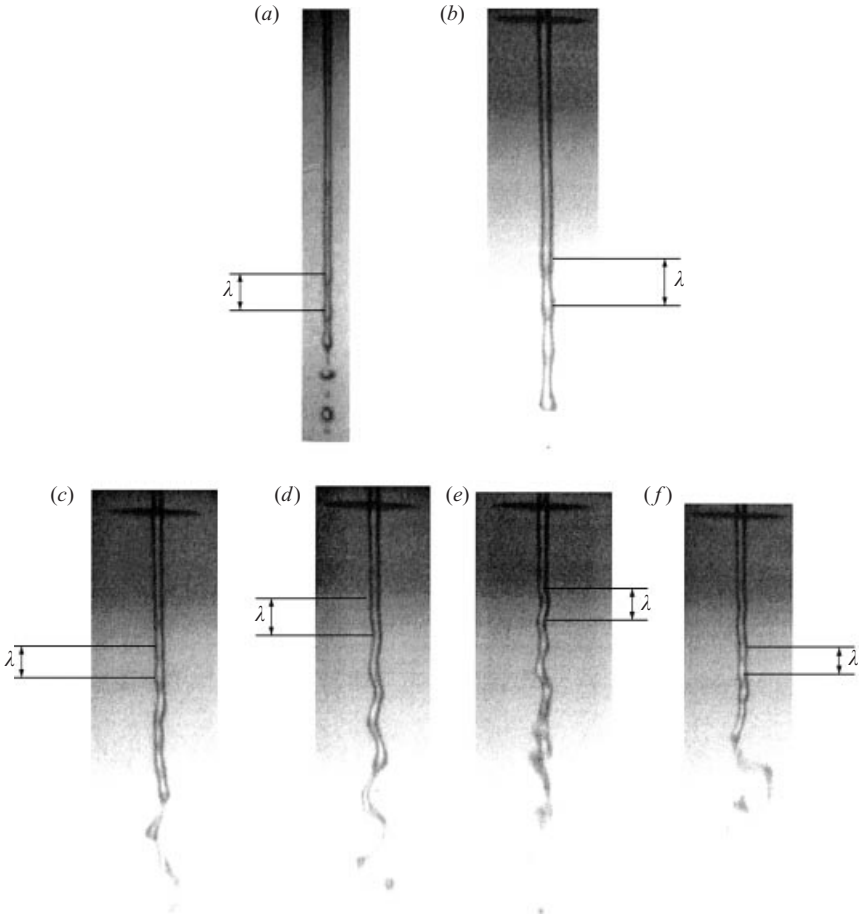

FIGURE 22. Photographs showing the different atomization regimes for a constant $Q = 30\,\mathrm{ml\,h^{-1}}$: (*a*) $\Delta p = 5$ KPa; $U_l = 3.2\,\mathrm{m\,s^{-1}}$; $U_g = 92\,\mathrm{m\,s^{-1}}$; $M = 800$; $Re = 233$; $We_0 = 6.3$; $\kappa = 0.68$; $z_r > 0.3$. (*b*) $\Delta p = 10\,\mathrm{KPa}$; $U_l = 4.5\,\mathrm{m\,s^{-1}}$; $U_g = 127\,\mathrm{m\,s^{-1}}$; $M = 739$; $Re = 295$; $We_0 = 11$; $\kappa = 0.77$; $z_r \sim 0.17$. (*c*, *d*) $\Delta p = 20\,\mathrm{KPa}$; $U_l = 6.3\,\mathrm{m\,s^{-1}}$; $U_g = 173\,\mathrm{m\,s^{-1}}$; $M = 638$; $Re = 387$; $We_0 = 20$; and for (*c*) $\kappa = 1.02$; $z_r \sim 0.13$; and for (*d*) $\kappa = 0.66$; $z_r \sim 0.12$; (*e*, *f*) $\Delta p = 30\,\mathrm{KPa}$; $U_l = 7.75\,\mathrm{m\,s^{-1}}$; $U_g = 208\,\mathrm{m\,s^{-1}}$; $M = 556$; $Re = 454$; $We_0 = 28$; and for (*e*) $\kappa = 0.68$; $z_r \sim 0.085$; and for (*f*) $\kappa = 1.21$; $z_r \sim 0.09$; (z_r denotes the non-dimensional breakup length).

rise to nearly uniform liquid velocity profiles without enough shear to promote the growth of the hydrodynamic and helicoidal modes. As Δp increases in figure 22(*b*) the liquid and gas streams accelerate and sharper boundary layers develop in both fluids, which leads to a breakup wavelength shorter than Rayleigh's. Breakup wavelengths shorter than Rayleigh's have also been predicted by previous works such as that of Lin & Chen (1998); however the modes that lead to the growth of short wavelengths in their investigation are, like those also present in our model A, due to the effect of gas inertia, whereas in our experimental situation the shear in the liquid is what controls the breakup process. This statement is supported by our numerical results if one takes into account that the effect of sharper boundary layers is equivalent to considering smaller values of z in figure 19, in which case the axisymmetric hydrodynamic modes grow faster than both the capillary axisymmetric and the helicoidal ones. The effect of non-uniformity of the velocity profiles strengthens for even larger Δp in

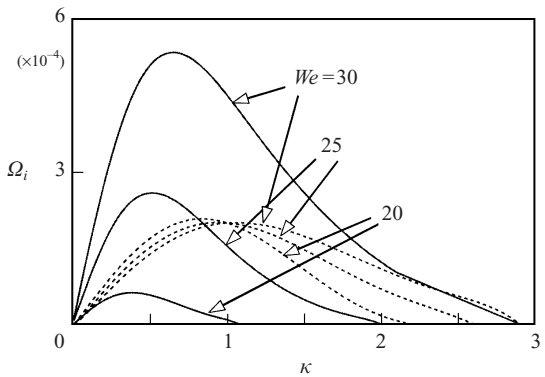

FIGURE 23. Growth rates of the hydrodynamic modes (dashed line) and helicoidal modes (continuous lines) for different values of the Weber number and for a fixed $M = 650$ at the section $z = 0.05$.

figure 22(c), for which the corresponding values of z in figure 19 are so low, and also the Weber number so large, that the capillary modes play no role in the breakup process which must be either of axisymmetric hydrodynamic or of helicoidal type. In fact, what we see in figure 22 is that, for the given Δp, the breakup mode is predominantly the axisymmetric hydrodynamic one (figure 22c) and the helicoidal one (figure 22d) occasionally overcomes the axisymmetric one. This can be easily explained on the basis of the numerical results shown in figure 23. For this We value, the axisymmetric mode still grows much faster than the helicoidal one. Notice also that the breakup wavelengths measured experimentally in figure 22(c, d), $\kappa = 1.02$ and $\kappa = 0.66$ respectively, are in qualitative agreement with the dispersion relation maxima shown in figure 23: the wavelengths of the helicoidal mode are larger than those that correspond to the hydrodynamic mode. One can also experimentally observe a sharp increase in the growth rate of the helicoidal mode for Weber numbers just above the experimentally measured $We = 20$, in agreement with theoretical predictions. As Δp increases further no new type of breakup process is observed; the instability mechanism is of hydrodynamic type and the jet breaks predominantly following a helicoidal mode (see figure 22e), while one may only occasionally observe the axisymmetric one (figure 22f). Since the way in which the jet breaks up depends on uncontrolled upstream perturbations which are convected downstream, and on nonlinear large-amplitude interactions with the surrounding gas stream, in these photographs we restrict ourselves to showing experimental evidence of the newly identified modes only qualitatively.

7. Conclusions

A linear temporal inviscid stability analysis of a liquid jet flowing with a coaxial gas stream has been performed. We have used in the analysis self-consistent basic velocity profiles obtained by integrating the coupled system of parabolized Navier–Stokes equations for both the gas and liquid streams formulated in § 2. As described in § 2, the integration has been carried out numerically with an easy-to-implement method of lines, and experimental results for the downstream evolution of the flow have served as a guide to choose appropriate values of the parameters characterizing the basic velocity profiles at the initial station (exit of the pressurized chamber) as explained in § 3. In a conventional way we have obtained in § 4 the set of linear

equations for the stability analysis, which we have applied to three different models in § 5.

The first model we have considered (§ 5.1) is that of a liquid jet of constant radius with uniform velocity profile surrounded by a gas stream which develops a boundary-layer-type velocity profile. We have found the same two types of modes, capillary and helicoidal, reported in the literature, but their growth rates strongly depend on the thickness of the boundary layer. In fact, for boundary layer thicknesses of the order of the jet radius (which is the most common situation in our experiments) the Kelvin–Helmholtz instability mechanism is not relevant, and the growth rates follow closely Rayleigh's curve in the case of axisymmetric disturbances (capillary modes), while the helicoidal modes have negligible growth rates. For thinner boundary layers we find the Taylor atomization regime (Lin & Chen 1998), but the existence of another length (δ) in the problem (Villermaux 1998) modifies substantially the growth rates obtained with the Kelvin–Helmholtz model. In fact, the classical Kelvin–Helmholtz dispersion relation is obtained only for the thinnest boundary layers; for larger thicknesses, but still small compared to the jet radius, the growth rates differ appreciably from Kelvin–Helmholtz results. Besides the capillary and helicoidal modes, there exists a third family of modes, which we have called *wake modes*, whose excitation frequencies are of the order of U_∞/R, which denotes their hydrodynamic origin, and their growth rates, which are of the order of those of the capillary modes, are not influenced much by the Weber number nor the boundary layer thickness.

In § 5.2 we have considered a second simplified model consisting of a liquid jet with a non-uniform velocity profile coupled to an external gas stream. In this case, in which we have assumed that the gas stream remains unperturbed under disturbances introduced in the liquid, the stability analysis reveals three different families of modes, two of them axisymmetric and the third one helicoidal. The first family of axisymmetric modes is of capillary type, and was also present in the previous model. The second family of axisymmetric modes, as well as the helicoidal family, are of hydrodynamic origin, as can be deduced from the behaviour of their growth rates which, for sufficiently high Weber numbers, increase with We and with the sharpness of the velocity profile. These modes, to our knowledge, have not been described previously in the literature.

Finally, in § 5.3 we have considered a more realistic model corresponding to the atomization experiments of figure 22. We have found essentially the same types of modes described for the two previous simplified models, although the growth rates are substantially modified with respect to the previous cases due to the influence of the structure of both liquid and gas basic velocity profiles and to the inclusion of perturbations in both streams. We have used the results of this model to explain the experimental results shown in figure 22(a–f) and concluded that, while for low gas velocities (low Δp) the breakup process is of capillary type according to Rayleigh's results, for larger Δp the hydrodynamic modes, axisymmetric and helicoidal, come into play and dominate the breakup process. Since the modes of hydrodynamic origin only appear theoretically when we consider the existence of a non-uniform velocity profile in the liquid jet, in our opinion no model including a trivial (constant) basic velocity profile in the liquid jet can describe correctly the breakup process in atomization experiments, at least in the case of gas-to-liquid momentum ratios close to one.

As a final remark we would like to stress once more the crucial role played by the basic flow in the stability analysis of parallel streams as pointed out by Lin & Reitz (1998), since both the type of modes to be predicted and their growth rates are very sensitive to it.

The authors are grateful to Drs Antonio Barrero Ripoll, Javier Dávila Martín, J. M. López-Herrera, M. A. Herrada and to Manuel González and J. L. Sampedro for useful discussions and comments on the manuscript and valuable experimental help. This work has been supported by the Dirección General de Investigación Científica y Técnica of Spain under projects PB96-0679-C02-02, PB96-1341, and partially by Kraft Foods Inc. and Aradigm Corp. J. M. G. is specially indebted to Dr Antonio Barrero for his support and continuous encouragement during this work.

REFERENCES

Arfken, G. B. & Weber, H. J. 1995 *Mathematical Methods for Physicists*, pp. 483–501. Academic.

Batchelor, G. K. & Gill, A. E. 1962 Analysis of the stability of axisymmetric jets. *J. Fluid Mech.* **14**, 529–551.

Gañán-Calvo, A. M. 1998 Generation of steady liquid microthreads and micron-sized monodisperse sprays in gas streams. *Phys. Rev. Lett.* **80**, 285–288.

Huerre, P. & Monkewitz, P. A. 1985 Absolute and convective instabilities in free shear layers. *J. Fluid Mech.* **159**, 151–168.

Keller, J. B., Rubinow, S. I. & Tu, Y. O. 1973 Spatial instability of a jet. *Phys. Fluids* **16**, 2052–2055.

Lasheras, J. C. & Hopfinger, E. J. 2000 Liquid jet instability and atomization in a coaxial gas stream. *Ann. Rev. Fluid Mech.* **32**, 275–308.

Lasheras, J. C., Villermaux, E. & Hopfinger, E. J. 1998 Break-up and atomization of a round water jet by a high-speed annular air jet. *J. Fluid Mech.* **357**, 351–379.

Leib, S. J. & Goldstein, M. E. 1986 The generation of capillary instabilities on a liquid jet. *J. Fluid Mech.* **168**, 479–500.

Li, X. 1995 Mechanism of atomization of a liquid jet. *Atomiz. Sprays* **5**, 89–105.

Lin, S. P. & Chen, J. N. 1998 Role played by the interfacial shear in the instability mechanism of a viscous liquid jet surrounded by a viscous gas in a pipe. *J. Fluid Mech.* **376**, 37–50.

Lin, S. P. & Kang, D. J. 1987 Atomization of a liquid jet. *Phys. Fluids* **30**, 2000–2006.

Lin, S. P. & Reitz, R. D. 1998 Drop and spray formation from a liquid jet. *Ann. Rev. Fluid Mech.* **30**, 85–105.

Miles, J. W. 1957 On the generation of surface waves by shear flows. *J. Fluid Mech.* **3**, 185–204.

Miles, J. W. 1959*a* On the generation of surface waves by shear flows. Part 2. *J. Fluid Mech.* **6**, 568–582.

Miles, J. W. 1959*b* On the generation of surface waves by shear flows. Part 3. Kelvin–Helmholtz instability. *J. Fluid Mech.* **6**, 583–598.

Miyazaki, T. & Kubo, T. 1995 Stability of a stretching capillary jet with parabolic axial velocity. *J. Phys. Soc. Japan* **64**, 3275–3283.

Rayleigh, Lord 1878 On the instability of jets. *Proc. Lond. Math. Soc.* **10**, 4–13.

Rayleigh, Lord 1880 On the stability or instability of certain fluid motions. *Proc. Lond. Math. Soc.* **11**, 57–70.

Rosenhead, L. 1963 *Laminar Boundary Layers*, pp. 446–451. Dover.

Sterling, A. M. & Sleicher, C. A. 1975 The instability of capillary jets. *J. Fluid Mech.* **68**, 477–495.

Villermaux, E. 1998 Mixing and spray formation in coaxial jets. *J. Prop. Power* **14**, 807–817.

Weber, C. 1931 On the breakdown of a fluid jet. *Z. Angew. Math. Mech.* **11**, 136–141.

Yang, H. Q. 1992 Asymmetric instability of a liquid jet. *Phys. Fluids* A **4**, 681–689.